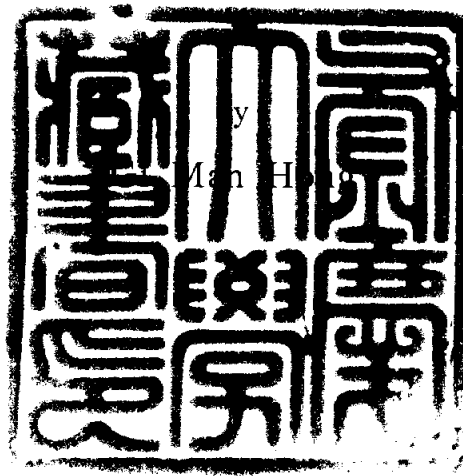


Retrieval of Meteorological Elements and Analysis of Heat Fluxes using Remote Sensing Data

원격탐사 자료를 이용한
기상요소 추정과 열플럭스 해석

Advisor : Prof. Young Seup Kim



A thesis submitted in partial fulfillment of the requirements
for the degree of

Doctor of Philosophy

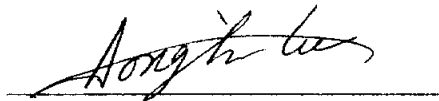
in the Department of Environmental Atmospheric Sciences,
The Graduate School
Pukyong National University

August 2004

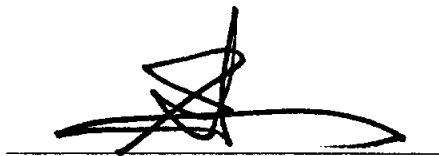
Retrieval of Meteorological Elements and Analysis
of Heat Fluxes using Remote Sensing Data

A dissertation
by
Gi Man Hong

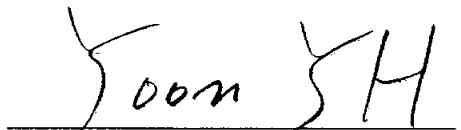
Approved by:



(Chairman) Dong In, Lee



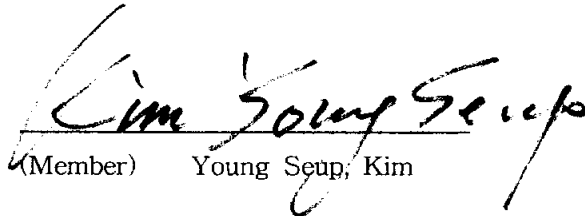
(Member) Hong Joo, Yoon



(Member) Yong Hoon, Yoon



(Member) Byung Hyuk, Kwon



(Member) Young Seup, Kim

August 31, 2004

원격탐사 자료를 이용한 기상 요소 추정과 열플럭스 해석

홍 기 만

부경대학교 대학원 환경대기과학과

요약

원격탐사를 이용한 대기-해양 상호작용의 메커니즘을 이해하기 위해 위성 자료 및 부이 자료를 이용하여 해양기상요소 추출 알고리즘을 개발하여 원격탐사에 의한 해양 기상요소 추출과 대기-해양 열교환 추정을 위한 알고리즘을 개선하였다. 새롭게 개선된 해양기상요소 추출 알고리즘과 대기-해양 열교환 추정 알고리즘을 이용하여 한반도 주변 해역의 열속 (현열속, 잠열속, 장파복사량, 단파복사량, 순열속)을 추정하고 검증하였으며, 이를 바탕으로 한반도 주변 해역에서 해양기상요소(해수면온도, 현·잠열 플럭스, 단파 및 장파 플럭스)를 표출시킬 수 있는 해양기상요소 표출시스템을 구축하였다.

위성에서 직접 관측할 수 없는 해수면 위의 기온을 추정한 결과 본 연구에서는 부이자료로부터 얻어진 해수면온도와 기온사이의 상관관계로부터 푸리에 급수 이용하여 좋은 결과를 얻을 수 있었다.

해수면 위의 비습 (Q)을 추정하기 위해 부이자료의 수증기압 (E_a)과 기온의 비선형 회귀식 관계로 산출한 3차 다중함수를 Schussel *et al.* (1995)이 SSM/I 경험식으로 얻은 결과와 비교·분석하였다. 분석 결과 Schussel *et al.* (1995)이 이용한 경험식보다 본 연구에서 제시한 비선형 회귀식에서 더 좋은 결과를 얻을 수 있었다.

한반도 주변 해역에서 대기-해양 열교환의 결과는 현열속의 경우에는 공간적인 분포 특징이 겨울철에 뚜렷하게 나타났고, 여름철은 현열속이 0에 가깝거나 음의 값을 보였다. 동해에서 현열속이 가장 컸고 다른 해역에 비해 수심이 낮은 서해의 경우 기온 변화에 대해 해수면 온도가 비교적 빨리 적응하여 온도차가 적어 현열속도 작게 나타남을 알 수 있었다. 잠열속은 대기가 건조해지고 바람이 강해지는 가을철에 최대가 나타나서 겨울철까지 지속되었다. 동중국해에서 잠열속이 가장 크게 나타났고, 서

해에서 가장 낮게 나타났다. 장파복사량은 해수면 온도와 기온차가 큰 동해에서 크고, 서해에서 낮은 값을 보였다. 단파복사량은 태양 고도에 따라 크게 영향을 받기 때문에 고위도로 갈수록 감소하는 분포를 보였으며, 일부 구름의 양이 영향을 미친 것으로 나타났다. 겨울철 순열속은 잠열속이 현열속에 비해 상대적으로 훨씬 더 크기 때문에 잠열속과 유사한 공간 분포를 보였다.

해양기상요소와 대기-해양 열교환에 대해 계절 변동과 연 변동성을 분석하였다. 해수면 온도와 기온의 경우 이미 알려진 바와 같이 겨울철에는 해수면 온도가 낮고, 여름철에는 높게 나타났으며 최대값은 8월, 최소값은 2월에 나타났다. 서해와 동해(또는 동중국해) 두 지역간의 해수면 온도차가 여름철보다 겨울철에 더 크게 나타났다. 가장 높은 해수면 온도는 1995년 동중국해에서 나타났고, 가장 낮은 해수면 온도는 1996년 서해에서 나타났다. 겨울철에 서해와 동중국해보다는 동해에서 풍속이 더 강하게 나타났고, 여름철에는 겨울철에 비해 풍속이 약해졌으며 동해에서보다는 서해와 동중국해에서 상대적으로 더 강한 풍속이 나타났다. 운량은 동해에서 0.6 이상으로 다른 해역에 비해 높게 나타났으며 전반적으로 봄철을 거쳐 여름철로 가면서 운량이 더 작게 나타남을 알 수 있었다. 또한 풍속의 경우 1989년 동해에서 최대로 나타났으며, 1989년에 최소값을 보였고 1992년 이후에 전체적으로 풍속이 증가하는 경향을 보였다.

열속 (현열속, 잠열속, 장파복사량, 단파복사량, 순열속)에 대한 계절과 연 변동 특징을 살펴보면, 현열속의 경우 여름철과 겨울철 현열속의 값이 극명하게 나타나고 분석기간 동안에 현열속은 1996년 겨울에 가장 높았다. 잠열속의 경우 9월에 값이 커지기 시작하여 1월에 최대값을 나타내며 순열속은 3월에서 9월까지의 양의 값을 보이고 10월부터 2월까지의 음의 값을 보였다. 단파복사량의 연 평균 분포는 같은 고도에 해양에서보다 대륙에서 왕성한 대류와 구름의 형성으로 인해 더 크게 나타났다. 장파복사량은 전 기간에 걸쳐 그 변동성이 작게 나타나고 겨울철에는 최대값을 여름철에는 최소값을 보였다.

연구기간 중에 사례연구를 통하여 현열속과 잠열속 그리고 난류에너지의 변화 형태에 대해서 분석하였다. 해수면 온도가 증가할 때 현열속은 감소하였고 잠열속과 난류에너지는 증가하였다. 이는 난류에너지 방정식에서 현열속이 감소하였다할지라도 잠열속의 증가에 비해 상대적으로 매우 작은 결과이기 때문에 난류에너지는 증가하였

다.

본 연구에 의해서 새롭게 개발된 해수면 위의 기온과 비습 추정을 통한 한반도 주변 해역 대기-해양 열교환의 추정과 해양기상요소 변동성 분석을 통해 앞으로 ENSO (El-Nino Southern Oscillation) 연구, 대기과 해양 순환의 이해, 대기·해양 순환 모델의 개선 등에 유용하게 쓰일 수 있을 것으로 기대된다.

I . Introduction

The ocean actively exchange heat, water and momentum with the atmosphere through the ocean surface. The exchanged heat, water and momentum are transported by the general circulation in the ocean and atmosphere to redress the heat imbalance. Since the exchange and transporting processes are essential components of the global climate, it is quite important to estimate these fluxes between the atmosphere and the ocean and of transports by ocean and atmospheric circulation to understand the mechanism of the global climate (Hirose *et al.*, 1999; Kubota *et al.*, 2002; Kim *et al.*, 2003). However, it is difficult to estimate those fluxes and transports globally using in-situ observation data from ships and buoys, since such data are extremely sparse in time and space. By contrast, we can obtain extremely homogeneous data with high resolution using analysis and satellite data.

The heat flux between the ocean and the atmosphere consists of four components, that is, shortwave radiation, longwave radiation, sensible heat and latent heat fluxes. Generally only shortwave radiation transfers heat from the atmosphere to the ocean, while the remaining three components transfer heat from the ocean to the atmosphere.

There are broadly method to estimate the shortwave radiation at

large scales. This method is a traditional method using empirical formulae to estimate the flux from surface meteorological observations such as air temperature, humidity and cloudiness. The longwave radiation flux at the sea surface has received less attention than the other components. One reason may be the difficulty in observing the longwave radiation flux due to the complicated formulae used in the estimation; furthermore, there are few reliable observation stations for the longwave radiation flux in the ocean. One way of estimating the longwave radiation flux at the sea surface is using satellite remote sensing data and applying a radiation-transfer model to estimate the flux. In most of the studies of this kind, empirical formulae that relate satellite observations to the outputs of sophisticated radiation-transfer models are used to obtain longwave radiation flux from satellite data; for example, SSM/I data, TOVS data, and ISCCP data.

Latent heat and sensible heat fluxes are globally estimated using a bulk formula for satellite data, which includes several kinds of physical variable, and the estimation of turbulent heat fluxes is complex. For this estimate, wind speed, specific humidity, and saturated specific humidity are necessary for latent heat, and wind speed, air temperature, and sea surface temperature (SST) are needed for sensible heat flux. In these necessary variables, specific humidity and air temperature are not easily obtained from satellite data compared with other data. Liu (1986), Schulz *et al.* (1993), and

Schlüssel *et al.* (1995) proposed an algorithm for estimating specific humidity from satellite data. Some studies proposed a method for estimating the surface level air temperature by satellite sensors (Kubota and Mitsumori, 1995; Konda *et al.*, 1996; Prihodko and Goward, 1997; Gautier *et al.*, 1998; Jones *et al.*, 1999). However, satellite-derived specific humidity and air temperature are not yet so accurate as to be satisfactory for the estimation of latent and sensible heat fluxes. In particular, air temperature is one of the most important elements of the climate parameters.

Monitoring the global distribution of surface-layer air temperature is important not only for evaluation the strength of thermal coupling between ocean and atmosphere but also for monitoring the long-term global warming and impact of the change of SST on it. The effort to improve the accuracy of satellite-derived air temperature should be encouraged.

The sparsity of observation data in time and space over the Korean Peninsula marginal seas has forced one to use climatological means of statistical methods to obtain information of the surface heat flux. Furthermore, most of the studies on the heat budget is limited to the East/Japan Sea area (Kato and Asai, 1983; Kim *et al.*, 1995; Kang *et al.*, 1994, Park *et al.*, 1995; Hirose *et al.*, 1999) due to the relative abundance of observations. Equivalent informations of the sea surface flux over the East/Japan Sea are limited in numbers reported over the Yellow Sea and East China Sea (Kim, 1992;

Hirose, 1995).

Even the climatological means of each component of the surface heat fluxes over the seas around the Korean Peninsula have been estimated by various scientists, the heat fluxes are significantly different because of the different bulk schemes and data sets. It has been known that the estimated values of heat flux are dependent on (1) the bulk formulas used to calculate the heat flux, (2) the type of data acquisitions and (3) the spatial and temporal resolution of the data set (Hsiung, 1986).

The purpose of this study lies in ascertaining the methodology of deriving highly accurate air temperature and specific humidity using the data by the oceanic meteorological buoys and satellites. Also, each component of the heat fluxes at the sea surface is evaluated using the bulk aerodynamic formulas, based on the satellite data from 1988 to 2000. Besides the seasonal and annual variation of heat fluxes at the Yellow Sea (YS), the East China Sea (ECS) and the East Sea (ES), more detailed features in all season when the heat exchange between the air-sea takes place actively.

II. Data

2.1 Satellite data

Basically we need sea surface temperature, air temperature, wind speed, cloudiness, specific humidity and saturation specific humidity to estimate sensible heat and latent heat fluxes by bulk formulae. However, saturation specific humidity can be derived by sea surface temperature observed by NOAA AVHRR MSCCT and wind speed and cloudiness data can be observed by DMSP SSM/I. Therefore, NOAA AVHRR and DMSP SSM/I data used in this study as satellite data.

We use the NOAA-NASA Oceans Pathfinder SST product (Brown *et al.*, 1993) rather than the optimal interpolated SST weekly analysis from Reynolds and Smith (1994), because the latter does not provide is derived from the five-channel AVHRR scanner that has been flown onboard the NOAA series of Polar Orbiting Operational Environmental Satellite (POESs) in sun-synchronous orbits since 1979. The five channels are located in the visible, near-infrared, and thermal infrared portions of the electromagnetic spectrum. Clouds have large effects on infrared measurements since they are opaque to infrared radiation and can effectively mask radiation from the ocean surface. Therefore, though the satellite orbits the earth 14

times each day from 833 km above its surface, and each pass of the satellite provides a 2399-km-wide swath, it usually needs 1 or 2 weeks, depending on the actual cloud coverage, to obtain a complete global coverage. The average SST retrieval has a root-mean-square-error (rmse) difference of around 0.5°C (McClain *et al.*, 1985). The daily field of the Pathfinder product is available with a spatial resolution of about 20 km × 20 km but with significant data gaps due to cloud.

The SSM/I has been operating since July 1987 onboard a series of Defense Meteorological Satellite Program (DMSP) spacecraft in a circular sun-synchronous near-polar orbit at an altitude of approximately 860 km and orbit period of 102 min. The 1394-km swath of the SSM/I, only half of that of AVHRR, covers 82% of the earth's surface between 87°36'S and 87°36'N in 24 h and produces a complete coverage within 3 days (Halpern *et al.*, 1994, Wentz, 1997) algorithm with a reference height at 10m is used. The data are available at a resolution of 12 h and at a swath resolution of 25 km. Wind speed values are also flagged if the measurements are within 50 ~ 100 km of the coast or within 200 km of the climatological mean monthly position of the ice edge because the validity of the algorithm is questionable over these areas. The SSM/I wind speeds have a rmse difference of 1.6 m/s and zero bias as compared to buoy measurements (Wentz, 1992). The Wentz's SSM/I product includes also total precipitable water over the open ocean. Schulz *et*

al. (1993) obtained the precipitable water in the lower 500 m of the atmospheric planetary boundary layer using the brightness temperature computed from the 19-GHz horizontal, and 19-, 22-, and 37-GHz vertical polarizations. By using estimates of the total and 0~500 m precipitable water, Chou *et al.* (1995) devised a retrieval technique to derive daily near-surface specific humidity based on the empirical orthogonal functions method. The derived surface humidity at 10 m has a rms difference of 1.83 gkg^{-1} estimated by SSM/I radiosonde comparison. Monthly fields with a spatial resolution of 1° latitude \times 1° longitude are provided from version 2 of the Goddard Satellite-Based Surface Turbulent Fluxes (GSSTF) data (Chou *et al.*, 2001).

Microwaves from the ocean have close links to the structure of waves and the roughness of the ocean surface, which are directly determined by winds adjacent to the oceanic surface (Wentz, 1992). As a result, the surface wind speed can be driven from the microwaves data (Hollinger *et al.*, 1990). Up to now SSM/I (Special Sensor Microwave/Imager) loaded in DMSP (Defense Meteorological Satellite Program) has been commonly used in the studies of oceanic surface wind speed (Yu *et al.*, 1997; Bennartz, 1999).

Recently, TMI (TRMM Microwave Imager) loaded in TRMM (Tropical Rainfall Measuring Mission), a satellite for joint project between the US and Japan, is being often used. TMI, composed of five channels (10.65 GHz, 19.35 GHz, 22.235 GHz, 37.0 GHz, 85.5

GHz), has horizontal resolution of 5 km (85.5 GHz) to 45 km (10.65 GHz), triple of SSM/I (65 km).

TRMM TMI comprises five channels which simultaneously observe microwaves emitted from the surface of the earth and the atmosphere. Four of TMI's channels (10.65 GHz, 19.35GHz, 37.0 GHz and 85.5 GHz) provide horizontal and vertical polarization observation while 22.235 GHz gives only vertical one. TMI antenna's caliber has scanning angle of 65 degree and swath width of 760km. The resolution of 10.65 GHz, 19.35 GHz, 22.235 GHz and 37.0 GHz are, respectively, 63×37 km, 30×18 km, 27×18 km, 16×9 km, narrower than that of 85.5 GHz (7×5 km).

2.2 Buoy Data

Ocean weather buoys that monitors weather condition or environment change over ocean are divided into moored buoy and drifting buoy. Moored buoys are the weather sentinels of the sea. They deployed in the coastal and offshore waters. Moored buoys measure and transmit barometric pressure, wind direction, speed and gust, air and sea surface temperature, and wave energy spectra from which significant wave height, dominant wave period, and average wave period are derived. Even the direction of wave propagation is measured on many moored buoys. As years go by, moored buoys play an important role in production of fundamental data that have

need of weather forecast on the ocean.

In this study, we used mostly various buoy around the Korean Peninsula and Japan Sea operated by KMA, JMA. Positions of eight buoys installed in the adjacent seas of Korean Peninsula and Japan sea are shown in Table 2: international buoy number #22101 (Dukjukdo), #22102 (Chilbaldo), #22103 (Geomundo), #22104 (Geoje), # 22105 (East Sea), #21002 (Tsushima current region of the southern part), #21004 (The southern part of the Japan), and #22001 (Kuroshio region) operated by JMA. The data of twelve variables have been taken regularly every hours and 3-hours. Four meteorological parameters (wind speed, air pressure, air temperature, and sea surface temperature) are used for estimating the heat exchange between the air-sea.

Table 1 and 2 show all satellite data source and their spatial resolution, and the attributes of buoy data, respectively. The monthly mean data are used for this study from Jan. 1988 to Dec. 2000. To minimize the potential error resulting from different heights of buoys. In the tables, each abbreviation means followings. DMSP: Defense Meteorological Satellite Program, SSM/I: Special Sensor Microwave/Imager, MCSST: Multi Channel Sea Surface Temperature, JMA: Japan Meteorological Agency, NDBC: US National Data Buoy Center, and TOGA-TAO: Tropical Ocean-Global Atmosphere-Tropical Atmosphere Ocean. Fig. 1 is map of the adjacent seas of Korean Peninsula showing the location of KMA and

JMA buoys and study area. The YS ranges from 33°N to 39°N in latitude and ranges from 120°E to 126°E in longitude. The ECS ranges from 27°N to 33°N in latitude and ranges from 120°E to 129°E in longitude. The ES ranges from 36°N to 40°N in latitude and ranges from 129°E to 135°E in longitude. The YS and the ECS are divided by line which join Cheju Island and Shanghai (southern part of the Yangtze River) in Chinese (Lee, 1999).

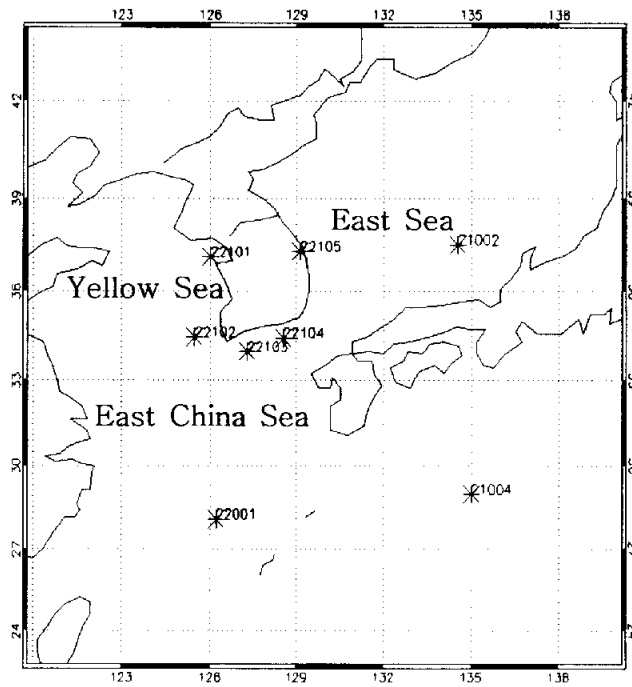


Fig. 1. Map of the adjacent seas of Korean Peninsula showing the location of KMA and JMA buoys and study area.

Table 1. Description of satellite data.

Source Data	Spatial Resolution	Retrieval Parameter
DMSP SSM/I	$1^{\circ} \times 1^{\circ}$	wind speed
DMSP SSM/I	$1^{\circ} \times 1^{\circ}$	cloudiness
MCSST	$0.175^{\circ} \times 0.175^{\circ}$	SST

Table 2. Description of KMA and JMA Buoys. Height is for the wind sensor.

Possessor	Buoy Number	Latitude(N)	Longitude(E)	Height(m)
KMA	22101	37.14°	126.01°	3.8
	22102	34.48°	125.47°	3.8
	22103	34.00°	127.30°	3.8
	22104	34.46°	128.54°	3.8
	22105	37.32°	129.12°	3.8
JMA	21002	37.55°	134.55°	7.5
	21004	29.00°	135.00°	7.5
	22001	28.10°	126.20°	7.5

III. Retrieval of meteorological elements

3.1 Air temperature, specific humidity and wind speed

In general, the atmospheric boundary near the sea surface has considerably homogeneous condition resulted from the continuous heat exchange between air-sea. Therefore, it could be assumed that air temperature has closely relationship with sea surface temperature.

Based on this assumption, we derive a corrected fourier series equation from the correlation between sea surface temperature and air temperature using the buoy data. Next step, sea surface temperature retrieved satellite data is substituted for that of a corrected fourier series equation. And then, air temperature obtained by the equation is validated by comparing with that of buoy data.

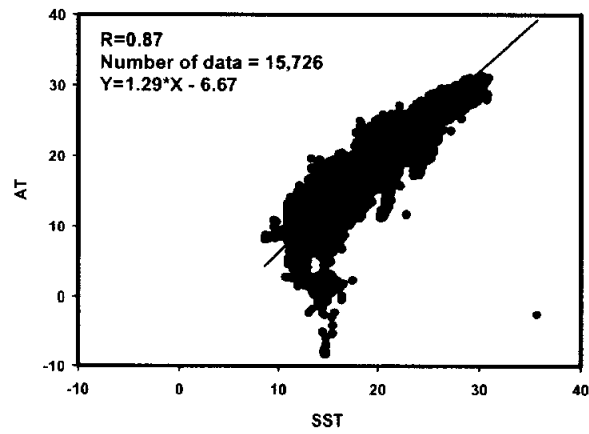
3.1.1 Air temperature

It is examined correlation between sea surface temperature and air temperature of buoy data to develop equation that estimate air temperature over the sea surface. Basically, Relationship of sea surface temperature and air temperature appeared in Fig. 2. The correlation coefficient is shown high correlation coefficient more than 0.87, however, it is very irregular form that seen in winter. This can

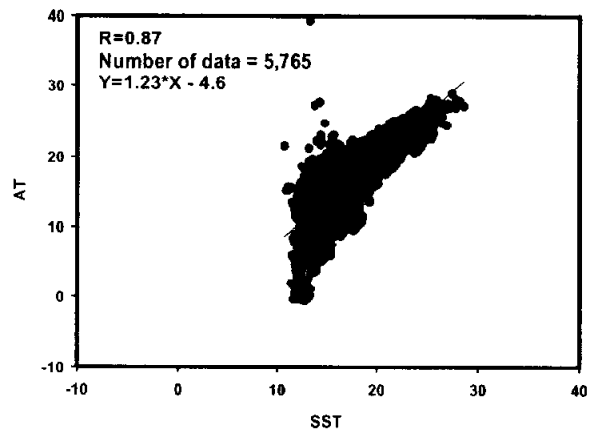
confirm even if Fig. 3. It must be improve this segment to estimate air temperature using sea surface temperature.

But, because stable value was seen in case of seize average more than 7 days in previous study, they have counted that particular problem does not exist. Fig. 4 displayed change of correlation coefficient that appeared when averaged AT data by time interval. When pass about 170 hours in JMA buoy as well as KMA buoy, it is seen very stable correlation coefficient more than 0.9. But, this can not reflect irregular form of air temperature in winter that appeared in Fig. 3.

Fig. 5 represents power spectral analysis of SST and AT using buoy data. In Fig. 5 (a), A small frequency fewer than 7 days frequency displayed regular form in SST data. But, in Fig. 5 (b), Could know that fairly irregular form appeared in small frequency than 7 days frequency. Thus, it must be consider certainly such irregular form in winter.

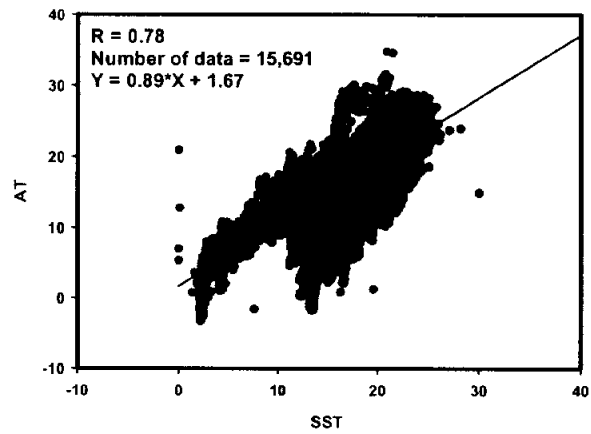


(a) Geomundo

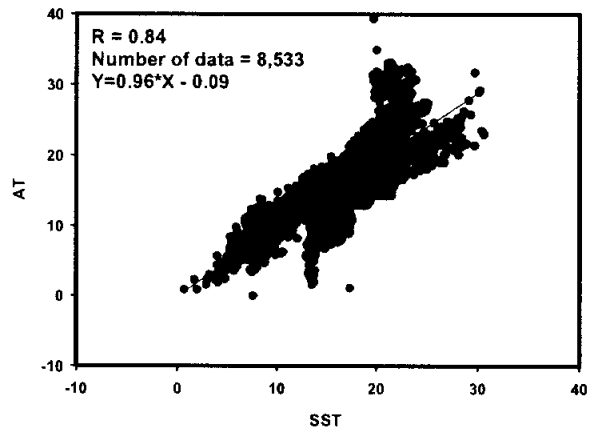


(b) Geoje-do

Fig. 2. Plots of the SST and AT measured from buoy data.



(c) Dukjukdo



(d) Chilbaldo

Fig. 2. (continued)

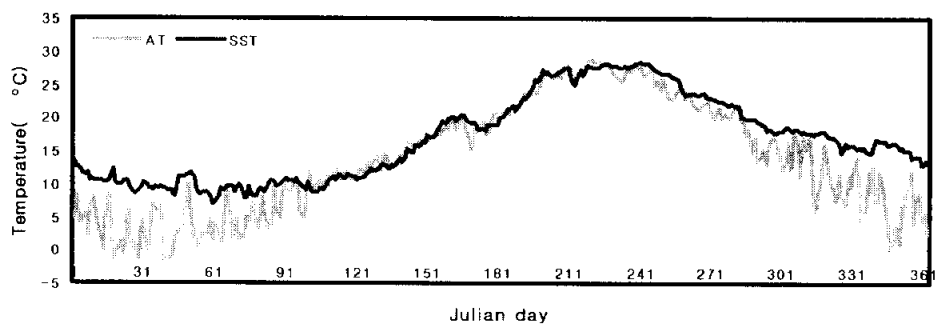
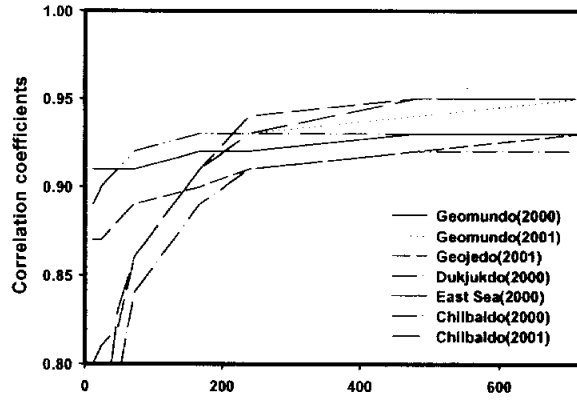
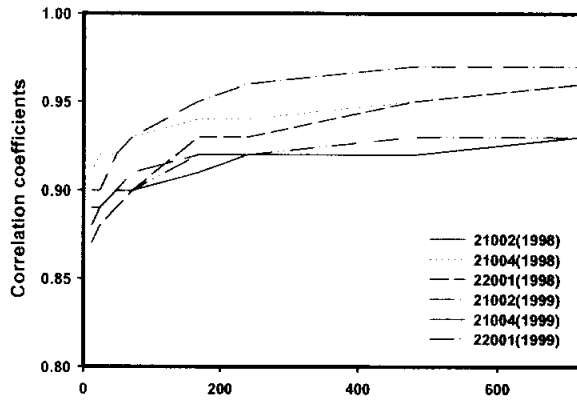


Fig. 3. Time series of SST and AT measured from buoy data.

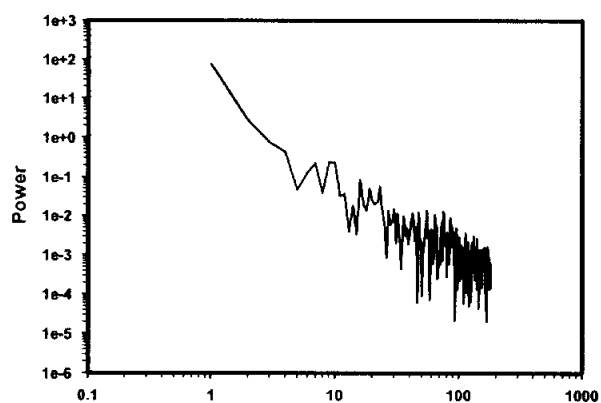


(a) KMA buoy

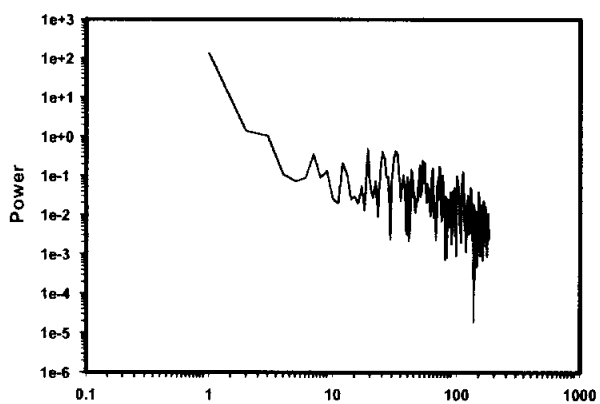


(b) JMA buoy

Fig. 4. Variation of correlation coefficient for hours from buoy data.



(a) SST



(b) AT

Fig. 5. Spectral power of SST and AT from buoy, respectively.

In this study developed AT retrieval equation to use Fourier Series. Definition of Fourier series is as following.

Let $f(x)$ be defined in the interval $(-L, L)$ [or $(0, 2L)$] and determined outside of this interval by $f(x+2L)=f(x)$, i.e. assume that $f(x)$ has the period $2L$ (it means that the starting point value is equal to the ending value). The Fourier series or Fourier expansion corresponding to $f(x)$ is defined to be,

$$f(x) = a_0 + \sum_{n=1}^{\infty} (a_n \cos nx + b_n \sin nx) \quad (3.1)$$

where the Fourier coefficients a_0 , a_n and b_n are

$$\begin{aligned} a_0 &= \frac{1}{2\pi} \int_{-\pi}^{\pi} f(x) dx \\ a_n &= \frac{1}{\pi} \int_{-\pi}^{\pi} f(x) \cos nx dx \quad n = 1, 2, 3, \dots, \infty \\ b_n &= \frac{1}{\pi} \int_{-\pi}^{\pi} f(x) \sin nx dx \end{aligned} \quad (3.2)$$

a_0 is mean value of $f(x)$.

If $f(x)$ has the period $2L$, the coefficients a_n and b_n can be determined equivalently from

$$f(x) = a_0 + \sum_{k=1}^{N/2} (a_n \cos \frac{\pi}{N} kx + b_n \sin \frac{\pi}{N} kx) \quad (3.3)$$

The Fourier coefficients a_n and b_n are

$$\begin{aligned} a_0 &= \frac{1}{N} \sum_{x=0}^{N-1} f(x) \\ a_n &= \frac{2}{N} \sum_{x=0}^{N-1} f(x) \cos \frac{\pi}{N} kx, & n = 1, 2, 3, \dots, N/2 \\ b_n &= \frac{2}{N} \sum_{x=0}^{N-1} f(x) \sin \frac{\pi}{N} kx \end{aligned} \quad (3.4)$$

Thus, this study can express to equation that can estimate AT applying Fourier series.

$$SST(t) = A_0 + \sum_{n=1}^{N-1} \sqrt{(A_n^2 + B_n^2)} \sin\left(\frac{2n\pi}{N} t + \theta\right) \quad (3.5)$$

$$AT(t) = a_0 + \sum_{n=1}^{N-1} \sqrt{(a_n^2 + b_n^2)} \sin\left(\frac{2n\pi}{N} t + \theta\right) \quad (3.6)$$

$$A_0 = \overline{SST}, \quad a_0 = \overline{AT}, \quad \sqrt{a_n^2 + b_n^2} = \sigma \sqrt{A_n^2 + B_n^2} + w$$

where t is Julian day.

Firstly, to estimate a_0 ,

$$AT(t) = SST(t) - \alpha(t - \beta), \quad \overline{AT}(t) = \frac{1}{N} \sum_{t=1}^N AT(t) \quad (3.7)$$

Thus, it can display AT by function of only SST by deciding a value. Also, it is decide to β value using below equation.

$$\begin{aligned} SST(t) - AT(t) = \overline{A_0 - a_0} + \sum_{n=1}^{N-1} [(A_n - a_n) \cos(\frac{2n\pi}{N}t) \\ + (B_n - b_n) \sin(\frac{2n\pi}{N}t)] \end{aligned} \quad (3.8)$$

$$\begin{aligned} \frac{d}{dt} [SST(t) - AT(t)] = \overline{A_0 - a_0} + \sum_{n=1}^{N-1} [(A_n - a_n) \cos(\frac{2n\pi}{N}t) \\ + (B_n - b_n) \sin(\frac{2n\pi}{N}t)] \end{aligned} \quad (3.9)$$

$$= \overline{A_0 - a_0} + \sum_{n=1}^{N-1} \frac{2n\pi}{N} [\sqrt{(A_n - a_n)^2 + (B_n - b_n)^2} \sin(\frac{2n\pi}{N}t + \theta)]$$

$$\theta = \cos^{-1} \frac{-(A_n - a_n)}{\sqrt{(A_n - a_n)^2 + (B_n - b_n)^2}} \quad (3.10)$$

It was decided to gradient of a value that can appear by difference of SST and AT. Also, β value decided difference of SST and AT to estimate that differential coefficient amounts to 0 when

did differential.

Thus, As to decide θ value, it was decided to AT estimation equation that developing in this study.

3.1.2 Specific humidity

Schlüssel *et al.* (1995) suggested an empirical formula to indirectly estimate the specific humidity by using SSM/I brightness temperature and sonde observation data. In the present study, unlike Schlüssel's method, we derive a regression equation from the correlation between air temperature and specific humidity by using buoy data, considering homogeneity of atmospheric boundary near the sea surface. And then, we replace air temperature with that obtained by the equation between sea surface temperature and air temperature. The result of this estimation is verified through the comparison with the other data.

3.1.3 Wind speed

It is of great importance to obtain observational data with simultaneousness and repetitiveness in the studies of oceanic surface wind, which has been, however, very difficult. Observation by marine probes vessel hardly produces repetitive oceanic data whereas mooring buoys cannot cover broad areas (Konda *et al.*, 1996). On

the other hand, satellites guarantee both simultaneous and repetitive data since they are capable of periodical observation over broad areas (Ulaby *et al.*, 1986; Shibata, 1992).

In order to validate the oceanic surface wind speed derived from TMI data, it is compared with the buoy data of NOAA NDBC (National Data Buoy Center) during the same period. Buoy data, with the error range of $\pm 0.5 \text{ ms}^{-1}$ to winds weaker than 10 ms^{-1} and $\pm 2 \text{ ms}^{-1}$ vis-a-vis those stronger than 10 ms^{-1} , has hourly average of 8.5 minutes. Buoy drifting more than 100 km away from the land is chosen to avoid the data contamination of oceanic brightness temperature (Table 3). To increase the validity of verification, corrected data of buoy winds and D-Matrix are taken only when TMI observation took place within 25 km from the location of the buoy and if TMI passed the area within 30 minutes since the buoy observed the wind speed. Since the speed sensor of NDBC buoy records the wind speed at the altitude of between 3 m to 10 m, to compare with TMI algorithm result, it is converted to a data equivalent to the altitude of 19.5 m using equation (3. 11).

$$\text{Wind speed } (M_2) = M_1 \times \frac{\ln(z_2/z_0)}{\ln(z_1/z_0)} \quad (3.11)$$

Wind speed (M_2) is defined to be zero at the ground (more precisely, at a height equal to the aerodynamic roughness length).

Speed increases roughly logarithmically with height, but the shape of wind profile depends on the surface roughness. Here, M_1 is wind speed of buoy, z_2 and z_1 are the altitude of 19.5 m and wind sensor height of NDBC buoy, z_0 (=0.002 m) is roughness length at the sea surface (Stull, 1995).

Table 3. Description of NDBC Buoys. Height is for the wind sensor.

Buoy	Number	Latitude (N)	Longitude (E)	Height(m)
NDBC	41001	34.68°	287.42°	6.0
	42001	25.92°	270.35°	10.0
	42002	25.88°	266.43°	10.0
	42036	28.50°	275.50°	3.0
	44004	38.45°	289.32°	6.0
	44011	41.08°	293.42°	6.0
	46002	42.52°	229.75°	6.0
	46003	51.85°	204.10°	6.0
	51002	17.18°	202.18°	6.0

It is by applying two data, TMI brightness temperature and buoy oceanic surface wind data identical to TRMM TMI observation on temporal and spatial basis, that we come up with oceanic surface wind speed algorithm. The algorithm used is empirical equation (3.12),

$$U = C_0 + C_1 T_B(19H) + C_2 T_B(22V) + C_3 T_B(37V) + C_4 T_B(37H) \quad (3.12)$$

DMSP wind speed retrieval D-matrix (Goodberlet *et al.*, 1989). The U (Oceanic surface wind speed) here is converted to a standard data equivalent to the altitude of 19.5m. The empirical equation (3.12) includes T_B , which represents the brightness temperature of the

frequency/polarization composition. H , V , and C respectively stand for horizontal polarization, vertical polarization and D-matrix.

3.2 Calculating of Heat Fluxes

The most practical method to estimate the heat fluxes in large scales is the bulk aerodynamic method which includes estimates of short and longwave radiations and sensible and latent heat fluxes with ordinary meteorological data. So far, climatological distributions of the heat fluxes in the wide regions over the world oceans were obtained by many authors (e.g., Bunker, 1976; Budyko, 1974; Reed, 1985; Hsiung, 1986) and seasonal variations of heat fluxes over oceans near Korean Peninsula and Japan by several authors (Miyazaki, 1952; Kato and Asai, 1983; Ishii and Kondo, 1987; Sakurai *et al.*, 1989, Kubota, 2002).

The net heat flux at the sea surface (Q_N) is given as

$$Q_N = Q_S - (Q_L + Q_H + Q_E) \quad (3.13)$$

where Q_S and Q_L are solar and longwave radiation flux, Q_H and Q_E are the sensible and latent heat fluxes, respectively. The solar radiation flux (Q_S) is estimated by

$$Q_S = Q_0(0.865 - 0.5C^2)(1 - \alpha_s) \quad (3.14)$$

$$Q_0 = A_0 + A_1 \cos \phi + B_1 \sin \phi + A_2 \cos 2\phi + B_2 \sin 2\phi \quad (3.15)$$

$$\phi = (t - 21) \times (2\pi/365) \quad , t = \text{Julian day}$$

where Q_0 is the solar radiation under the clear sky (Seckel and Beaudry, 1973) (refer to Table 4), C is the amount of cloud in tenths, α_s is the albedo at the sea surface ($=0.06$). The longwave radiation flux (Q_L) is calculated according to the formula (Clark *et al.*, 1974)

$$Q_L = \epsilon\sigma T_s^4(0.39 - 0.00495e_a^{0.5})(1 - \delta C) + 4\epsilon\sigma T_s^3(T_s - T_a) \quad (3.16)$$

where ϵ is the emissivity of water ($=0.97$), σ is the Stefan-Boltzman constant ($=5.6705 \times 10^{-8} \text{W/m}^2\text{K}^{-2}$), δ is the cloud coefficient which is a function of latitude and it is varying from 1.0 at the poles to 0.5 at the equator (Berliand and Berliand, 1952) (refer to Table 5) and e_a is the vapor pressure, and T_s and T_a are the sea surface and air temperature, respectively.

Monthly values of the latent (Q_E) and sensible (Q_H) heat fluxes are estimated by the bulk formulas with Kondo's transfer coefficients (1975) as follow:

$$Q_H = \rho_a C_P C_H U (T_s - T_a) \quad (3.17)$$

$$Q_E = \rho_a L C_E U (q_s - q_a) \quad (3.18)$$

In Eqs. (3.17) and (3.18), ρ is the air density, C_P is the specific

heat of air at constant pressure, U is the wind speed, L_v is the latent heat of evaporation, q_a is the specific humidity and q_s is the saturated specific humidity at T_s . Wind speed is derived from the empirical equation that Goodberlet *et al.* (1989) ascertained based on SSM/I data. C_H and C_E are the transfer coefficient for the sensible and latent heat flux and determined by wind speed and atmospheric stability are taken from the work of Kondo (1975). The meanings of the variables and constants in the formulas are summarized in Table 6.

Table 4. The coefficient for the solar radiation under clear sky (Seckel and Beaudry, 1973).

coefficient	latitude 20°S to 40°N	latitude 40°N to 60°N
A_0	$-15.82 + 326.87 \cos L$	$342.61 - 1.97L - 0.018 \cos L^2$
A_1	$9.63 + 192.44 \cos(L+90)$	$52.08 - 5.86L + 0.043L^2$
B_1	$-3.27 + 108.70 \sin L$	$-4.80 + 2.46L - 0.017L^2$
A_2	$-0.64 + 7.80 \sin 2(L-45)$	$1.08 - 0.47L + 0.011L^2$
B_2	$-0.50 + 14.42 \cos 2(L-5)$	$-38.79 + 2.43L - 0.034L^2$

Table 5. Mean latitudinal values of the cloud coefficients for the Eqs.(3.14) (Berliand and Berliand, 1952).

lat	75°	70°	65°	60°	55°	50°	45°	40°
δ	0.82	0.80	0.78	0.76	0.74	0.72	0.70	0.68

lat	35°	30°	25°	20°	15°	10°	5°	0°
δ	0.66	0.63	0.61	0.59	0.57	0.55	0.52	0.50

Table 6. Values of the variables and constants in equations: I_0 and δ are referred to in Seckel and Beaudry(1973), Reed(1977), and Berliand and Berliand(1952).

Parameter	Symbol	Value
Solar radiation under the clear sky	I_0	Wm^{-2}
Amount of Cloud	C	0-1
Albedo at the sea surface	α_s	0.06
Emissivity at the sea surface	ε	0.97
Stefan-Boltzmann constant	σ	$5.6705 \times 10^{-8} \text{Wm}^{-2}\text{K}^{-4}$
Air temperature	T_a, θ_a	$^{\circ}\text{C}, \text{K}$
Sea surface temperature	T_s	$^{\circ}\text{C}$
Vapor pressure	e_a	hPa
Cloud coefficient	δ	0.60-0.69
Air density	ρ_a	$1.290-1.305 \text{ Kg m}^{-3}$
Specific heat of air	c_a	$1004.6 \text{ J Kg}^{-1}\text{C}^{-1}$
Bulk transfer coefficients	C_h, C_e	(-)
Wind speed	W	ms^{-1}
Latent heat of evaporation	L	$2.50-2.57 \text{ J Kg}^{-1}$
Specific humidity	q_a	(-)
Saturated specific humidity at T_s	q_s	(-)

IV. Validation of meteorological elements

4.1 Air temperature (AT)

Multi-Channel Sea Surface Temperature (MCSST) by the satellite observation are examined by the comparative verification with buoy observation sea surface temperature (SST). Air Temperature (AT) is related to buoy-observed SST regardless of seasonal changes by the following Fourier series equation,

$$AT(t) = SST(t) - \alpha(t - \beta) + \sum_{n=1}^{N-1} (\sigma \sqrt{a_n^2 + b_n^2} + w) \sin \frac{2n\pi}{N} t + \theta \quad (4.1)$$

where t is Julian day, α is the gradient of difference between SST and AT, β is inflection point. α is a function of day and it is varying from -0.048 to 0.065.

Fig. 6 shows variation of SST gradient with latitude and month. SST gradient showed greatly according as latitude rises in winter season, and SST gradient showed almost changelessly in summer season. It was seen in Fig. 7 to show montlyly SST gradient from this result. SST gradient was the biggest in March and the value is about -1.5. SST gradient from June to August was almost regular

as explained in previous, and appeared sinusoidal function on the whole. α obtained by Fig. 6 and Fig. 7 are -0.048 and 0.065 , respectively. β is 200 day ($0.5^{\circ}\text{C} < \Delta T < 1.0^{\circ}\text{C}$).

Fig. 8 shows plots of power of SST and power of AT obtained from buoy data. In this paper obtained σ and ω value from relation equation by Fig. 8. σ and ω are 0.62 and 0.034 , respectively. Thus, by substituting MCSST for SST in (4.1), we can indirectly derive AT, which has turned out to produce better coefficient (0.95), BIAS (0.28°C) and RMSE (1.5°C) compared with the result of McClain *et al.* (1985) as illustrated in Fig. 9.

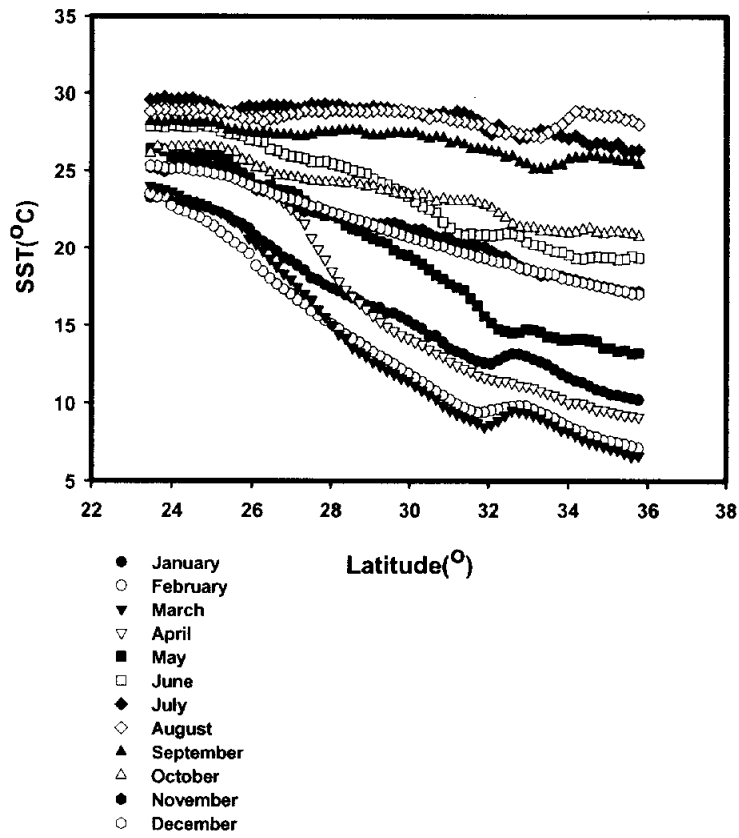
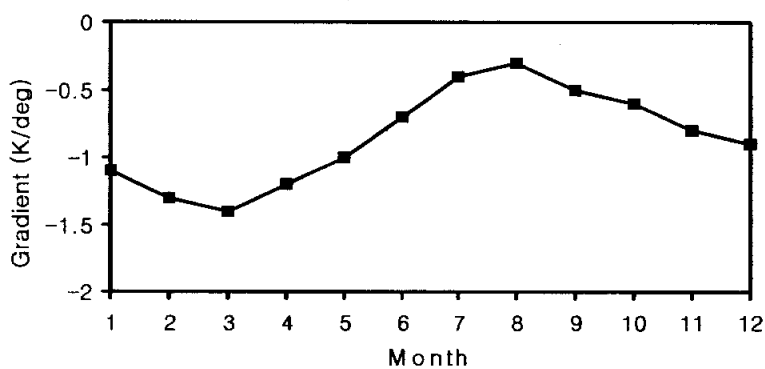


Fig. 6. Variation of SST gradient with latitude and month.



$$SST(t) = -0.55 \sin\left(\frac{\pi}{6}\right)t - 0.85$$

Fig. 7. Seasonal variation of monthly SST gradient.

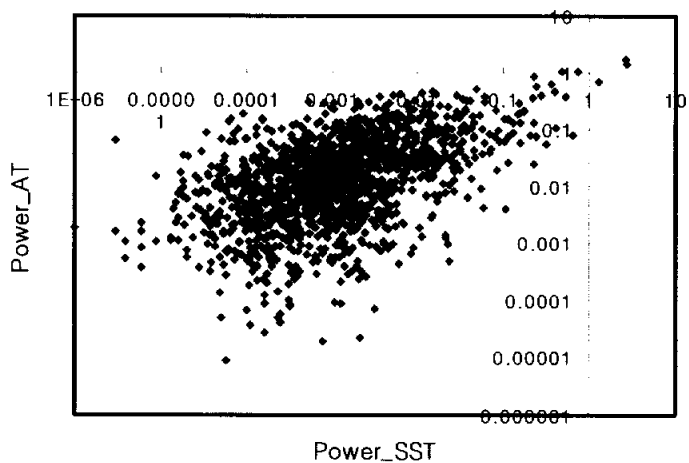


Fig. 8. Plots of power_SST and power_AT obtained from buoy data.

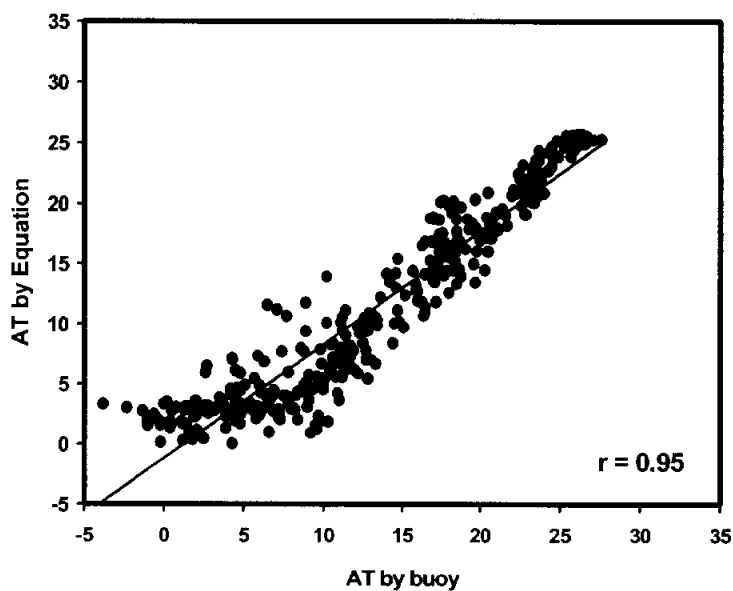


Fig. 9. Comparison of the air temperature derived from newly developed equation with that from buoys data.

4.2 Specific humidity (q_a)

As with SST, sea surface specific humidity (q_a) is hard to directly observe by satellites due to restrictions of radiative air transfer (Shibata *et al.*, 1996). q_a can be written as ratio of vapor pressure (e_a) to atmospheric pressure (p).

$$q_a = \frac{\varepsilon \cdot e_a}{p} \quad (4.2)$$

in which ε is 0.622 g/g and vapor pressure (e_a) is a function of air temperature. Vapor pressure is not to be directly observed by satellite and thus should be derived from non-linear regression equation. Buoy-observed monthly average vapor pressure and AT during the year of 1997 present a non-linear regression equation, which is a three dimensional function illustrated in formula (4.3). Fig. 10 shows good relationship between the values.

$$e_a = 0.0007 \times (AT)^3 + 0.0079 \times (AT)^2 + 0.3504 \times (AT) + 4.5980 \quad (4.3)$$

The substitution of AT obtained from formula (4.1) in formula (4.3) helps generate vapor pressure with only satellite-observed data. Fig. 11 and Fig. 12 are a scatter plot of buoy-observed specific humidity and specific humidity calculated from the regression

equation (4.3). The scatter plot diagram indicates that the regression equation has produced a good result of BIAS (-1.42 g/kg) and RMSE (1.75 g/kg), even better than specific humidity Schlüssel *et al.* (1995) obtained by using SSM/I satellites. In addition, the results include better correlative coefficient and RMSE than Jang *et al.* (1999), which was 0.95 and 1.77 g/kg respectively. Moreover, the comparison of the results with the NCEP/NCAR reanalysis data illustrates BIAS (-0.26 g/kg) even better than satellite and buoy-observed data but generated disappointing RMSE (6.22 g/kg). This is mainly due to the local limitations of NCEP/NCAR reanalysis data and any future use of NCEP/NCAR reanalysis data should thus take it into consideration.

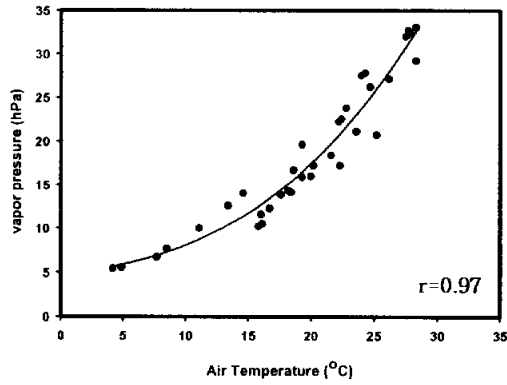


Fig. 10. Statistical regression between vapor pressure and air temperature obtained from buoys data.

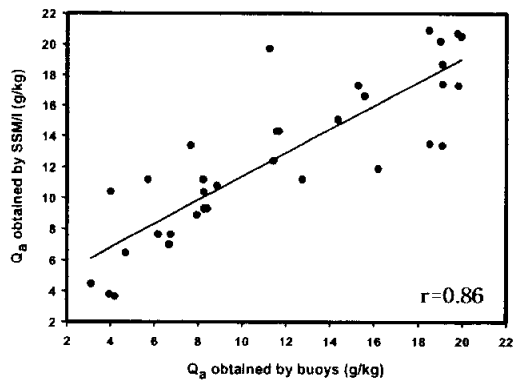


Fig. 11. Comparison of Q_a (specific humidity) the obtained by buoy data and that of retrieved from SSM/I satellite.

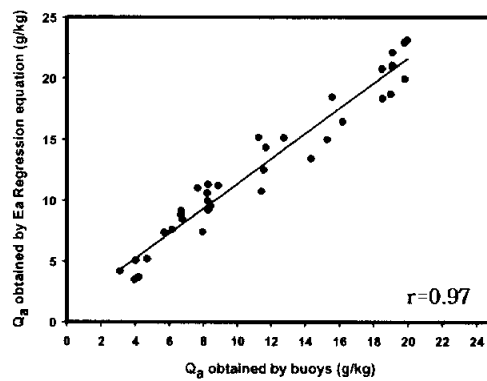


Fig. 12. Same as Fig. 11. but for regression equation.

4.3 Wind speed

This study adopts the empirical equation (3.12). As specified in Table 7, the coefficient with the utmost correlation is applied to the retrieval of oceanic surface wind speed.

We have retrieved oceanic surface wind speed in the vicinity of the North American continent by processing DMSP wind speed retrieval D-matrix algorithm to TRMM TMI brightness temperature data. Fig. 13 is a scatter plot showing the comparison between the oceanic surface wind speed from buoy data and the one retrieved from TRMM TMI data. The comparison of July and November data shows correlation coefficient of 0.81, RMSE is 2.19 ms^{-1} , and the bias is 1.10 ms^{-1} (refer to Table 8). The correlation coefficient is slightly smaller than the value(0.84) by Jang *et al* (1997) using SSM/I retrieval method while the bias has decreased by 0.42 ms^{-1} . Fig. 13 also indicates that wind speed stronger than 10 ms^{-1} tends to cause somewhat overestimated result. Fig. 14 illustrates a distribution of wind speed in May, July and November derived from TRMM TMI data. According to Fig. 14, November has stronger wind speed than May and July and the highest speed derived during these periods is approximately 13 ms^{-1} . Overall result of this study has similar trends shown in the previous studies while we admit that our study leads to somewhat overestimated result. Fig. 15 shows that wind speed estimated from

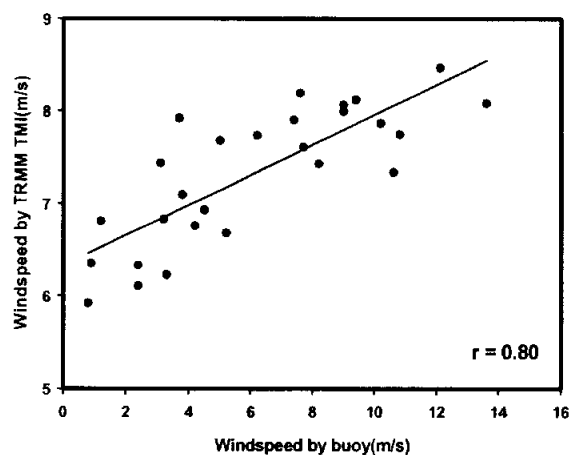
TRMM TMI data is overestimated in comparison with NCEP/NCAR reanalysis data but still has trends similar to Fig. 14.

Table 7. Coefficient and relative performance of the best global multichannel D-matrix algorithms.

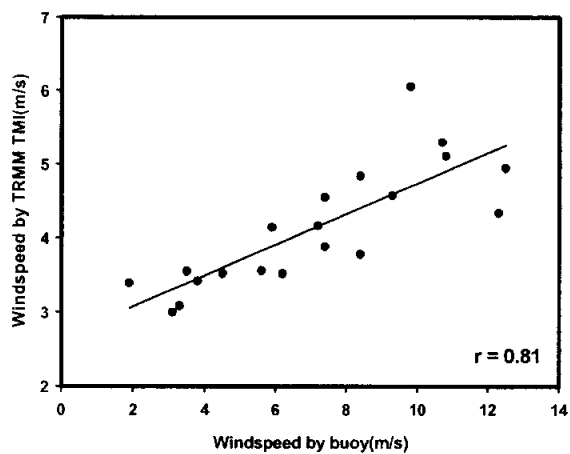
Coefficient		19 <i>V</i>	19 <i>H</i>	22 <i>V</i>	37 <i>V</i>	37 <i>H</i>	
C_0	48.1536	-	-0.1017	-0.2425	0.3127	-0.1816	0.81
C_1	51.8556	-0.4115	0.1836	-	0.1728	-0.1735	0.75
C_2	45.8727	-0.5493	0.3549	0.0085	-	0.0106	0.56
C_3	54.8144	-0.3874	0.2367	-0.2582	0.1740	-	0.58

Table 8. Statistical comparison of the TRMM TMI and NDBC buoy wind speed. r is correlation coefficient.

Name of source data	Mean (ms ⁻¹)	RMSE	BIAS	r
NDBC Buoy	6.24	2.19	1.10	0.81
TRMM TMI	7.34			



(a) July



(b) November

Fig. 13. Comparison of the surface wind speed derived from TMI data with that from NDBC buoys, (a) July and (b) November, 1998.

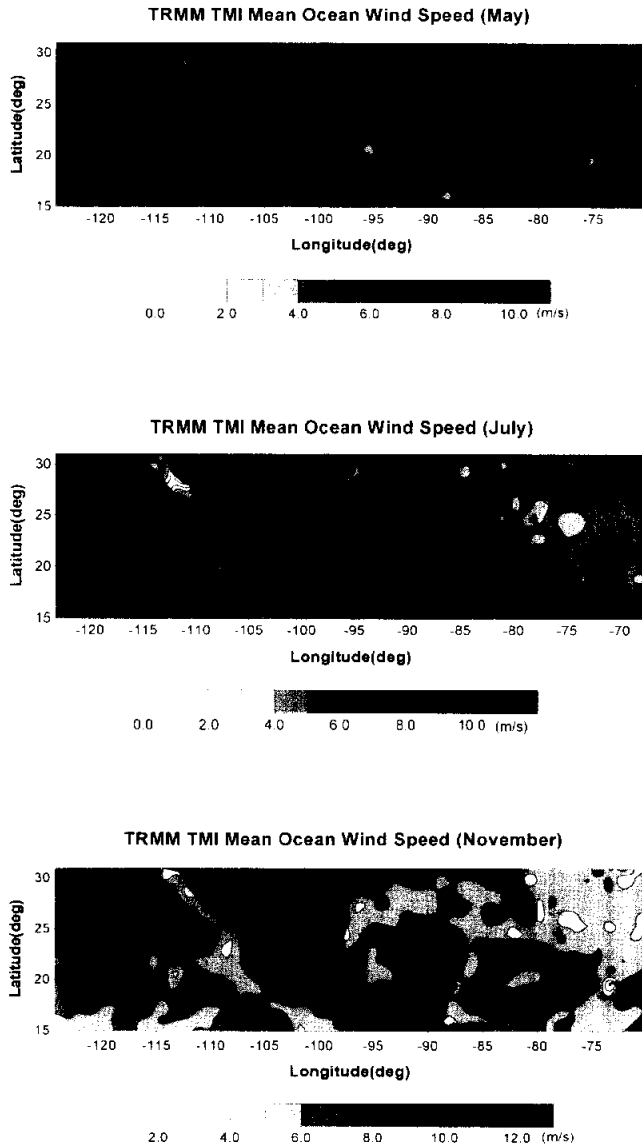


Fig. 14. Distribution of oceanic surface wind speed in the study area estimated from TRMM TMI data, (a) May, (b) July and (c) November, 1998.

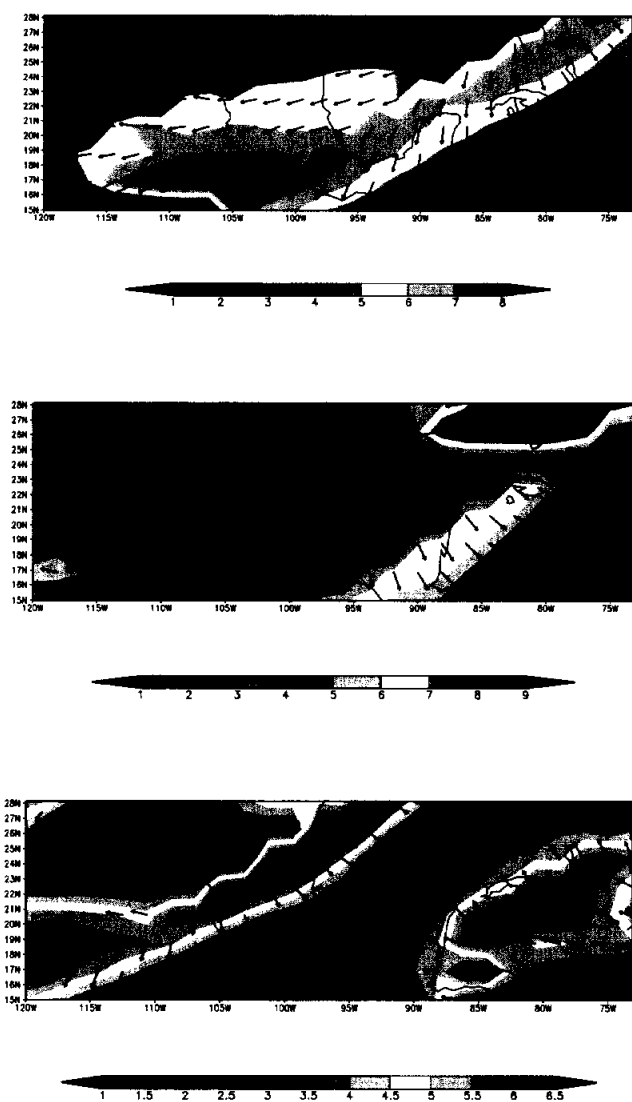


Fig. 15. Averaged wind speed and direction from NCEP/NCAR Reanalysis data, (a) May, (b) July and (c) November, 1998.

4.4 Heat fluxes

The meteorological element required for the bulk formula of sensible and latent heat flux estimation is satellite-observed data, which is to be verified through a comparison with buoy observation data. However it is of little significance to compare the heat flux estimated from satellites observation with that from buoys around Korea and Japan. In its stead, we calculate sensible heat and latent heat flux by utilizing AT and specific humidity derived from the above illustrated regression equations, MCSST data from the area around Korea and Japan ($23^{\circ}\text{N} \sim 44^{\circ}\text{N}$, $120^{\circ}\text{E} \sim 140^{\circ}\text{E}$), and finally wind speed from SSM/I data. The heat flux is then compared with NCEP/NCAR reanalysis data from the same area. Table 9 shows a statistical analysis of the retrieved heat flux along with the results of other preceding studies. Since the statistical figures are based on different areas and data categories, it is hardly feasible to compare the annual average of heat flux in each study. However it is still noteworthy that the estimated values show 40 to 50% of difference. Chou *et al.* (1995) took up EOF method for the humidity estimation and derived monthly average of latent heat flux, of which the RMSE ranged from 20 to 60 W/m^2 . Our study's RMSE of latent heat flux coincides with the mid-point of the result in Chou *et al.* (1995). Shibata *et al.* (1996) used the Bowen ratio between latent heat flux and sensible heat flux and estimated heat flux from the

satellite-observed data. Their BIAS of heat flux was slightly overestimated recording positive value. On the other hand, our study's heat flux BIAS, estimated from satellite-observed data, recorded negative as in Jang *et al.* (1999). The average of sensible heat flux derived from our study has recorded the same with the result of Jang *et al.* (1999) but showed very small error (Table 9) while the average of latent heat flux is more than one and half of the results of Jang *et al.* (1999) with similar RMSE and BIAS.

Fig. 16 shows the comparison between monthly averages of (1) heat flux estimated from the observational data of the satellite located at the same spots as three JMA buoys in the vicinity of Korea and Japan and (2) heat flux from NCEP/NCAR analysis data. To obtain (1), AT and Q_a for summer season (Apr. to Sep.) and winter season (Oct. to Mar) were calculated respectively. This is to minimize the error caused by different regression equation for SST and AT in summer season and in winter season. Thus (1) fairly well depicts seasonal changes and substantially corresponds to NCEP/NCAR reanalysis data. On the other hand, the reanalysis data of heat flux in January and August records extraordinarily higher than the satellites data, which accounts for the large RSME of heat flux (19.8 W/m^2) in Table 9. The high sensible heat flux in August is explained by synoptic weather phenomena as typhoon and seasonal rain while the one in January is a consequence of Kuroshio current around Japan. As NCEP/NCAR reanalysis data is

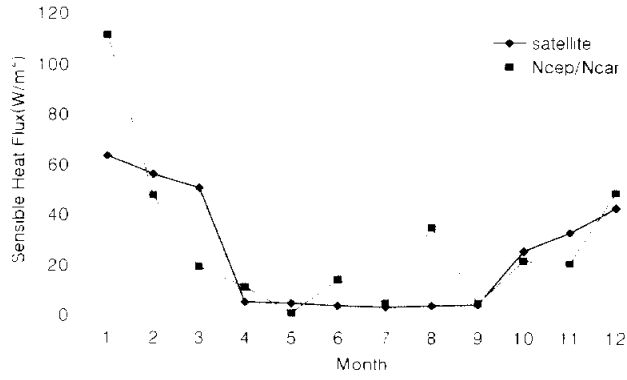
interpolation of horizontal resolution grids around the buoys and thus tends to be easily influenced by intensive weather phenomena or currents, which accounts for exaggerated sensible heat flux in January and August. The kind of exaggeration is also apparent in latent heat flux recorded from December to February. The values show difference of more than 40 W/m^2 from satellite-estimated data and produces huge error (44.2 W/m^2) in Table 9. This means Kuroshio current affects changes not only in temperature but also in humidity.

Table 9. Comparisons with previous results for heat fluxes (W/m^2).

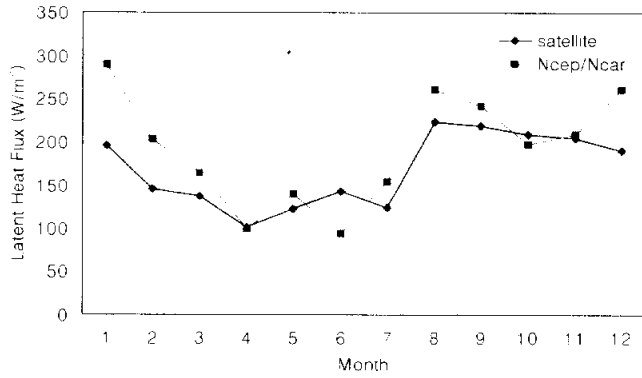
References	Latent Heat Flux			Sensible Heat Flux		
	Mean	RMSE	BIAS	Mean	RMSE	BIAS
Chou <i>et al.</i> (1995)		20 ~ 60*				
Shibata <i>et al.</i> (1996)		37.6*	19.0		8.7	5.4
Jang <i>et al.</i> (1999)	108	49*	-25	26	16	-6
Present Study	167.8	44.2**	-24.8	24.5	19.8	-3.5

* The values are compared with between buoy and satellite.

** The value is compared with between satellite and NCEP/NCAR reanalysis data.



(a) Sensible Heat Flux



(b) Latent Heat Flux

Fig. 16. Comparison of the Heat Flux obtained by satellite data with retrieved from NCEP/NCAR reanalysis data. (a) Sensible heat flux, (b) Latent heat flux.

V. Heat fluxes over the seas around Korean Peninsula

5.1 Evaluation of meteorological elements

5.1.1 Seasonal variations

Monthly mean of the wind speed is shown in Fig. 17 during 13 years (1988 to 2000). The strongest wind speed appeared in January and the maximum value of 13.96 ms^{-1} occurred at the ES in Korean Peninsula and the northwest area of the Japan Sea. In winter season, the wind speed is stronger at the ES than at the ECS and the YS. However, in summer season, the wind speed at the ECS and the YS are relatively stronger than at the ES. The monthly mean values of the wind speed are about $7\sim 9 \text{ ms}^{-1}$ over the seas around the Korean Peninsula.

Monthly mean of the cloudiness is shown in Fig. 18 during 13 years (1988 to 2000). The monthly mean distributions of the cloudiness showed that the maximum value occurred in January at the ES. The largest value is seen at the ES more than average cloudiness 0.6 in January, and July showed small value as 0.3. Tendency of general cloudiness could know that cloudiness is smaller from April to July. Because this is related to longwave radiation, longwave radiation showed large in July and showed small

in January. Sohn (1996) investigated that the effect of cloud gets for longwave radiation balance of atmosphere upper part and surface of the earth. As a result, cloud is heating atmospheric layers through longwave radiation in Tropical region, while cloud clears atmospheric layers that bring the effect of cooling in subtropical anticyclone area of middle latitudes cold region. That is, results of atmosphere heating by cloud coincides with total heating distribution by diabatic process including latent heat flux, sensible heat flux and longwave radiation. This is doing static contribution to a part of whole diabatic process conclusion that is doing insinuation.

Fig. 19 shows seasonal variations of sea surface temperature for the ECS, the YS and the ES. In the case of sea surface temperature, seasonal variations of three regions (ECS, YS and ES) showed small in winter season and showed large in summer season. Sea surface temperature had maximum (29.2°C) in August and minimum (8.3°C) in February at all of the three regions. Also, sea surface temperature showed that the YS is less on the whole than the ECS or the ES according to area. Because this is effected a lot of impacts by cold outbreak in winter at the YS (Ahn, 1997). The YS and the ES (or the ECS) can see that difference of sea surface temperature shows more greatly in winter than in summer.

In the case of air temperature, this study showed seasonal variations of result that is assumed by itself estimation algorithm development method. That is, air temperature assumed by method

that use fourier series equation divides into each applicable fourier series equation in winter and summer again and applied. In this study, in winter season applied from September to March, and in summer season applied from April to August. Like this, when reason that should apply dividing estimates sensible heat and latent heat flux, because difference of sea surface temperature and air temperature are interacted on important elements, because the value changes greatly whether September is come in winter or is come in summer. Fig. 20 shows seasonal variations of air temperature. As shown in this figure, the maximum appeared in January and the minimum appeared in February. The whole tendency also has deep related with sea surface temperature.

In estimating to heat fluxes in the ocean, one among important element is wind speed in the ocean. Specially, sensible heat and latent heat flux showed different values by intensity of wind speed in the ocean, when estimate sensible heat and latent heat flux, applied empirical formula of Kondo (1975) that consider effect of wind speed in the ocean to apply bulk transfer coefficient.

Fig. 21 shows seasonal variation of wind speed over the ocean in Korean Peninsula. Wind speed in the ocean of 10 ms^{-1} is blowing in winter similarly with sea surface temperature and air temperature, and wind speed in the ocean of 4 ms^{-1} is blowing in June as minimum values. This result is reflected well in result of analysis of the sensible heat and latent heat flux in next section. Sensible heat

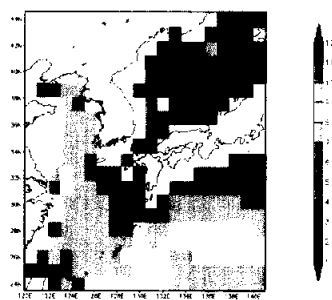
and latent heat flux for wind speed in the ocean showed large in winter and sea style displayed small value in summer. Also, because ocean wind speed decreased suddenly in September and the reason that September is included in fourier series equation of winter.

Cloudiness is external appearance aspect ratio for all sky of segment that is covered to cloud and shows by 10 fractions and divides 0 to 1. When cloudiness is 0 as clear sky, and cloudiness is 1 as dark sky. Generally among heat fluxes in the ocean, cloudiness affects most greatly influences on the longwave radiation and the shortwave radiation flux. That is, the longwave radiation was large in winter that there are a lot of cloudiness in general and the shortwave radiation was small, while the longwave radiation is small in summer that cloudiness is less and the shortwave radiation is large.

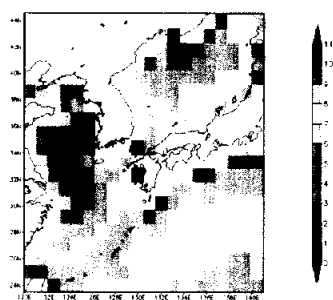
Fig. 23 and Fig. 24 showed correlation of cloudiness and longwave radiation and shortwave radiation flux. The correlation coefficient between longwave radiation and cloudiness was 0.61. As there are a lot of cloudiness, longwave radiation showed positive correlation. However, the correlation coefficient between the shortwave radiation and cloudiness was 0.64. As there are a lot of cloudiness, shortwave radiation showed negative correlation.

Fig. 22 shows seasonal variations of cloudiness. Seasonal variations is not seen but cloudiness is large in winter in general, and can know that cloudiness showed small in summer, also

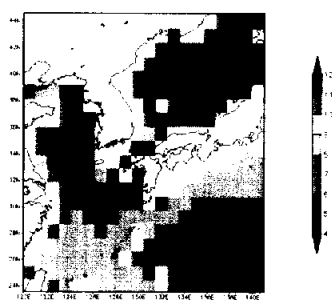
cloudiness is smaller at the YS than the ECS or the ES around the Korean Peninsula. But cloudiness shows relatively larger in June than in July and in August. This is related with rainy season in Korea. Especially, cloudiness showed large at the ECS and the ES over the seas around the Korean Peninsula.



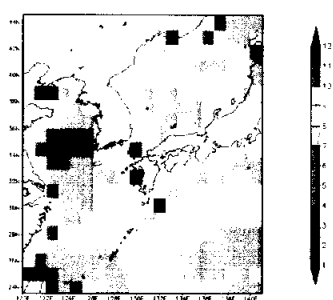
(a) January



(b) April

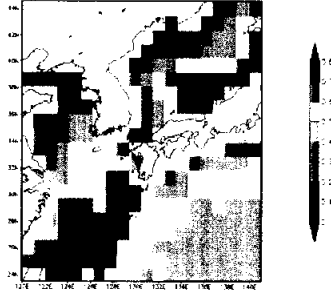


(c) July

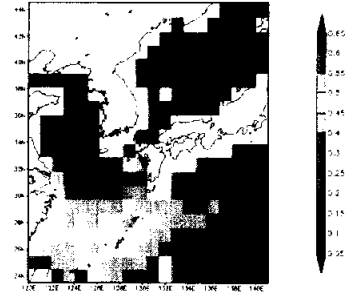


(d) October

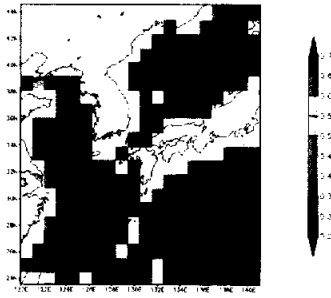
Fig. 17. Monthly mean wind speed in ms^{-1} from 1988 to 2000.



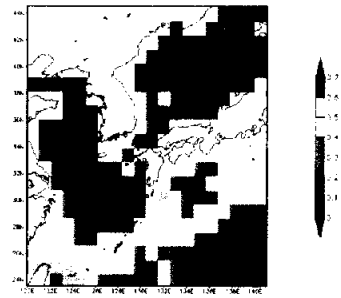
(a) January



(b) April



(c) July



(d) October

Fig. 18. Same as Fig 17, but for cloudiness in tenth.

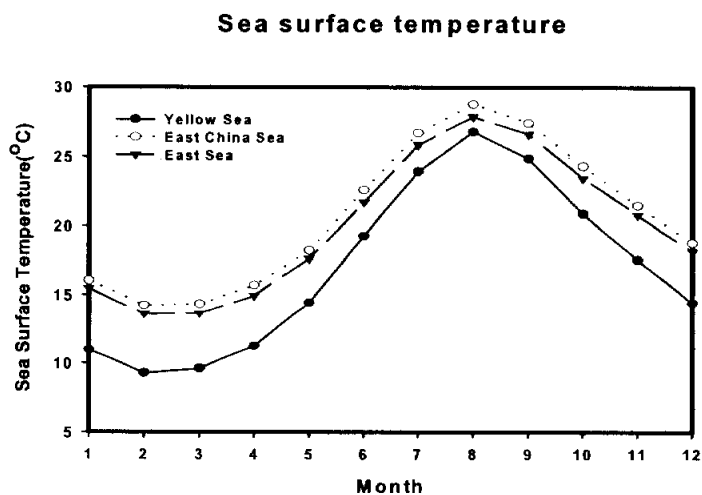


Fig. 19. Seasonal variation of the sea surface temperature around the Korean Peninsula.

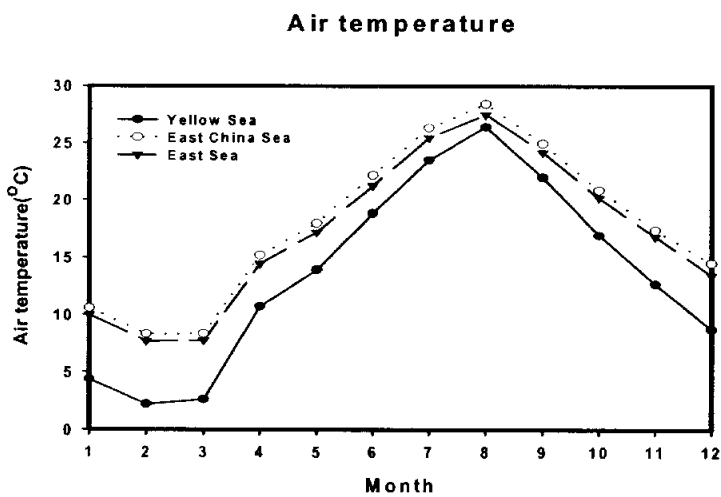


Fig. 20. Same as Fig. 19. but for air temperature.

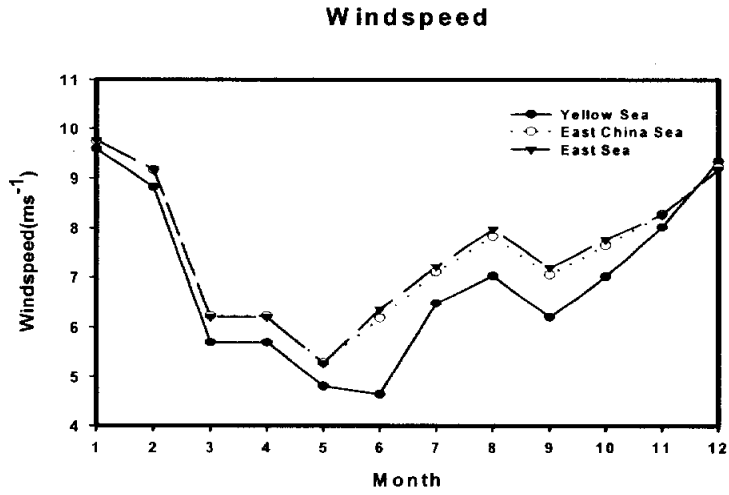


Fig. 21. Same as Fig. 19. but for wind speed in ms^{-1} .

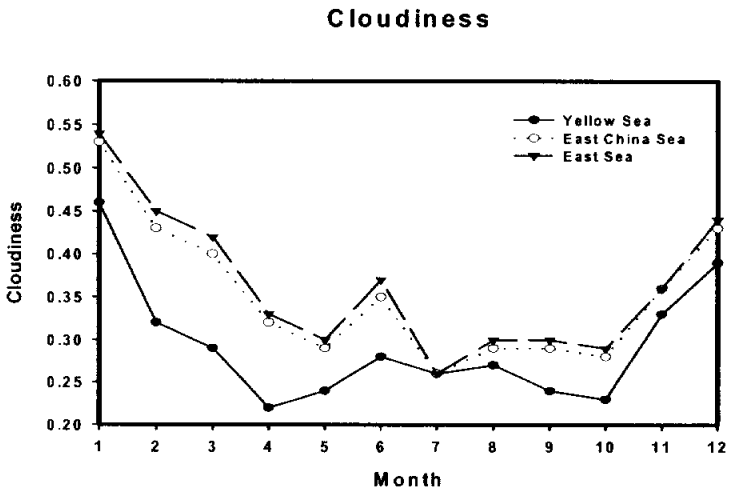


Fig. 22. Same as Fig. 19. but for cloudiness in tenth.

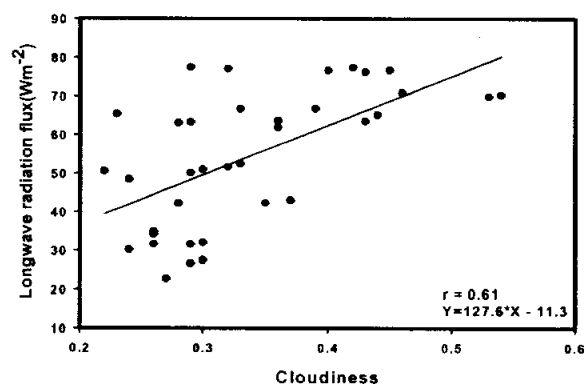


Fig. 23. Relationships of the cloudiness and longwave radiation flux.

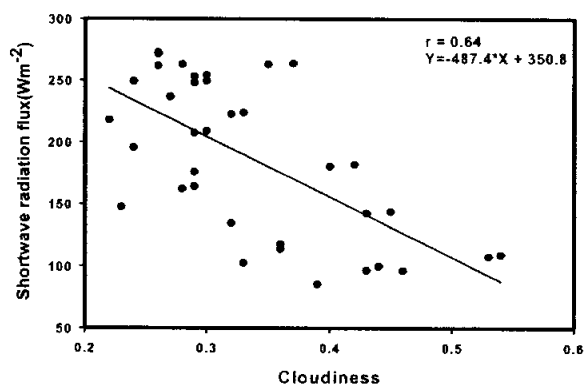


Fig. 24. Relationships of the cloudiness and shortwave radiation flux.

5.1.2 Annual variations

Annual variations for oceanic meteorological elements (sea surface temperature, air temperature, wind speed, cloudiness etc.) have been studied deeply by a lot of researchers. Shibata *et al.* (1996) controls exchange of sensible heat and latent heat flux, and analyzed Tropical Pacific Ocean's ENSO (El-Nino Southern Oscillation) phenomenon in heat exchange process by air-sea interaction. Also, Wallace and Blackmon (1983) cleared that variations of sea surface temperature is mostly effected by the atmospheric circulations. Ahn *et al.* (1997) was shown similarity that oscillation appeared greatly relatively, and displayed strong oscillation in 13-15 months cycle commonly long period more than several years in occasion of sea surface temperature and air temperature in period analysis. Announce that sea surface temperature and air temperature displayed anomaly of positive and negative each in winter and summer at opening part during study period and anomaly of a positive and negative showed each in winter and summer of latter.

Fig. 25 showed annual variations (1988 to 2000) of sea surface temperature over the seas around the Korean Peninsula. The ECS and the ES changed the annual mean values of a range of 12 ~ 27°C, while the YS changed lower about the annual mean values of 5°C than the ECS and the ES. Amplitude of annual variations showed most greatly at the YS. The year that is shown most sea

surface temperature between 1988 and 2000 years appeared by annual mean about 27.2°C (ECS) by 1994 and the year that is shown the lowest sea surface temperature was occurred by annual mean about 7°C (YS) by 1996. Fig. 26 shows annual variations (1988 to 2000) of the air temperature over the seas around the Korean Peninsula. Air temperature appeared lower about annual mean 5°C than sea surface temperature on the whole. Because seasonal variations changed slowly in the ocean.

Wind speed in the ocean is one of external cause that movement of water mass. Therefore, variations of sensible heat and latent heat flux in the ocean depends on according to the intensity of wind speed and exerts a lot of effects in whole energy equilibrium. Fig. 27 shows annual variations (1988 to 2000) of the wind speed over the sea around the Korean Peninsula. As shown Fig. 27, Wind speed showed more strongly about 2 ms^{-1} at the ECS and the ES than at the YS. Wind speed appeared to maximum value (11.7 ms^{-1}) at the ES in 1991 and in 1988 displayed minimum value at the YS. This is result by cold air outbreak that happen at YS in winter. Annual variations of wind speed increased on the whole since 1992.

Fig. 28 shows annual variations (1988 to 2000) of the cloudiness over the seas around the Korean Peninsula. Usually, cloudiness is closely connection with shortwave radiation. In the Fig. 28, cloudiness appeared the highest is 1990 and the value is about 0.73

and the lowest in 1995 and the value is about 0.08. Also, Annual variations of cloudiness was shown very irregular aspect than other meteorological factors.

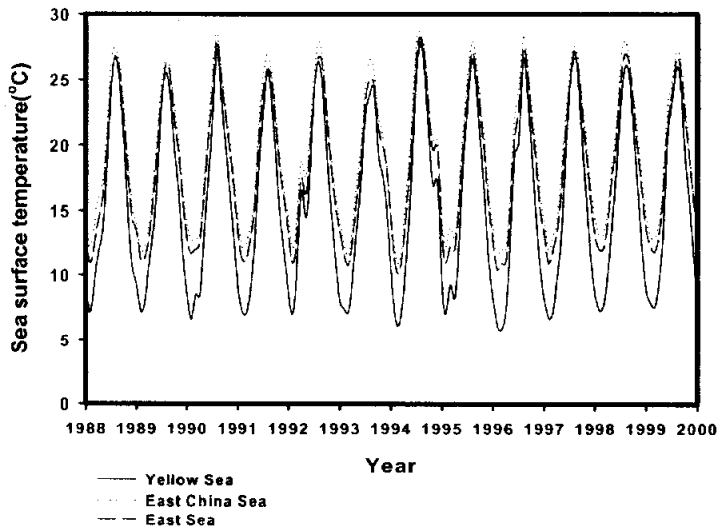


Fig. 25. Annual variation of the sea surface temperature around the Korean Peninsula.

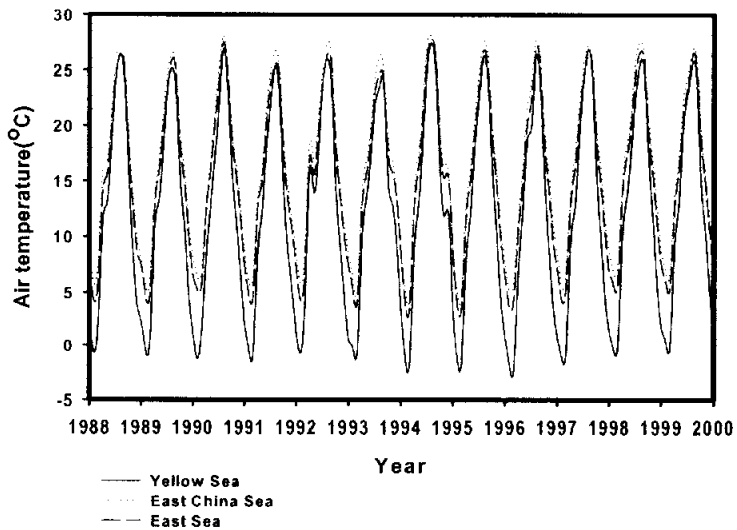


Fig. 26. Same as Fig. 25, but for air temperature.

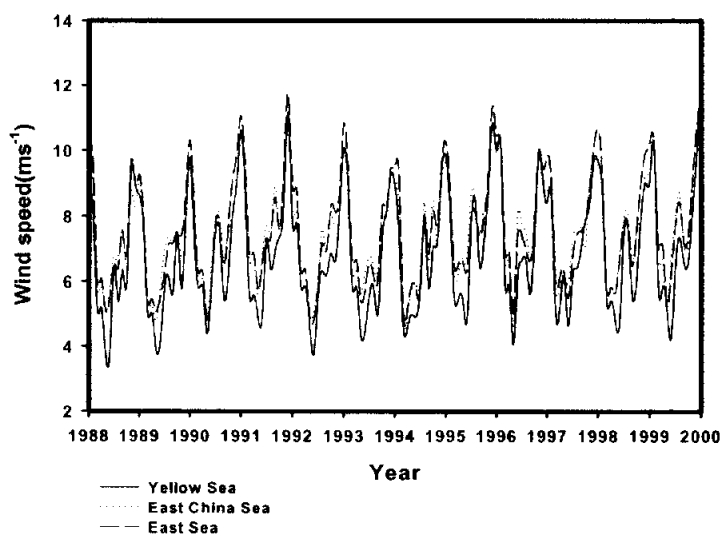


Fig. 27. Same as Fig. 25. but for wind speed.

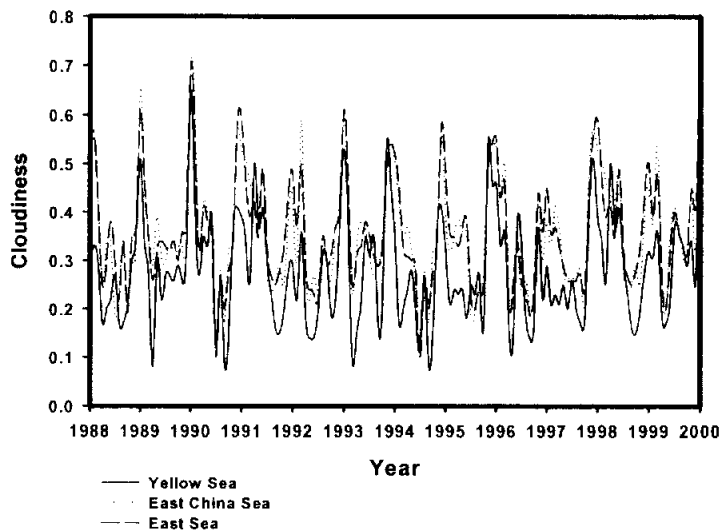


Fig. 28. Same as Fig. 25. but for cloudiness.

5.2 Evaluation of sea surface heat fluxes

5.2.1 Seasonal variations

Sensible heat flux means ratio of sensible heat transport that pass certain squares. For example, sensible heat transported to perpendicular direction during unit time passing put unit area to do horizontality into atmosphere is sensible heat flux of perpendicular direction. If it estimates annual mean energy balance in global surface, sensible heat flux emits about 5% of annual mean great besides that solar radiation (about 338 Wm^{-2}) from sea surface to atmosphere. Generally, seasonal variations of sensible heat flux over the ocean effected greatly on difference between sea surface temperature and air temperature. Thus, sensible heat flux appeared large in winter and small in summer. Latent heat flux means a heat transfer from sea to the atmosphere through evaporation process. Latent heat flux in the ocean shows maximum from autumn season to winter season.

Longwave radiation is infrared radiation that emits soil, atmosphere and cloud. Because temperature of land surface or temperature ranges from 200 to 300 K, there is energy of longwave radiation in area more than $4 \mu\text{m}$ wavelength. Generally, seasonal variations of longwave radiation emitted from atmosphere to ocean is as function of differences between sea surface temperature and air

temperature, temperature difference is large in winter and is small in summer. Usually, the radiation less than 4 μm wavelength is known as shortwave radiation. To be below 4 μm among radiation observing on earth almost whole solar energy be influenced. Shortwave radiation is shown distribution that decrease as go to high latitude and horizontal difference causes to difference of cloudiness.

The monthly mean values of surface heat flux are obtained from satellite data at each grid point. In order to examine the seasonal variations of each component of sea surface heat fluxes, except net heat flux (Q_N) of every month, the representative month for each season (January, April, July and October) is selected and the results are presented in Fig. 29 through 33.

Spatial variations of the net heat flux(Q_N) are shown in Fig. 29. In summer, the ECS, the ES and the YS gain heat almost uniformly as shown in Fig. 29. Incoming solar radiation is dominant in the net heat fluxes in this season. The net heat flux begins to decrease in October almost everywhere. The maximum monthly heat loss occurs in December or January due to the strong upward turbulent fluxes. This large loss of heat means that the warmer water is sufficiently cooled down by the colder air in this region. Similar to the turbulent flux showss in the eastern part of the ECS except during summer. This local maximum of the upward net heat flux also showed in some previous studies (Ishii and Kondo 1987; Kang *et al.*, 1994).

The strong gradient of the heat fluxes is formed in the northwestern part of the ECS (Fig. 29).

The net heat flux increases from February while keeping the horizontal gradient until May. The reverse net heat flux occurs from March in the northern part to May over the Kuroshio current. The strong annual loss of heat exceeding 150 Wm^{-2} occurs over the Kuroshio current. This indicates that much heat advected from the Tropics is lost to the atmosphere in this region. In the vicinity around the boundary between the YS and ECS, the net heat flux is larger for the western side than for the eastern side.

Fig. 30 shows spatial distribution of monthly mean shortwave radiation flux in the study area. The shortwave radiation decreases as is going to high latitude in winter (January) and is bigger relatively in winter than in summer (July). Because this is smaller cloudiness values of the summer season and incoming shortwave radiation is influenced greatly according to solar altitude, it is shown distribution that decrease as go to high latitude. The values cause in difference of cloudiness.

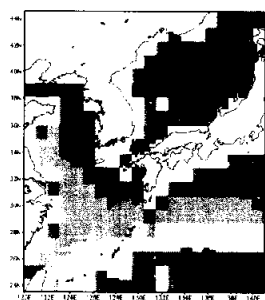
Spatial distribution of monthly mean longwave radiation flux is shown in Fig. 31. Let's examine whole spatial distribution in this study area. Longwave radiation appears to maximum at southeast seashore over the Korean Peninsula and Japanese Sea. This was involved that sea surface temperature is large being influenced at Kuroshio Current (Ahn, 1997). In the Korean Peninsula surrounding

seas area, difference of sea surface temperature and air temperature showed large at the ES and showed small at the YS. This is because longwave radiation is function of temperature difference.

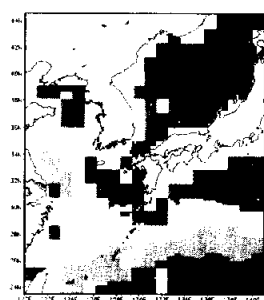
Fig. 32 shows spatial distribution of monthly mean latent heat flux radiation in the study area (1988 to 2000). Latent heat flux in the ocean shows maximum from autumn season to winter season. The maximum area of latent heat flux coincided almost with maximum area of specific humidity difference. Latent heat flux showed large at the ES and the value of annual mean is 108.6 Wm^{-2} , while latent heat flux showed small at the YS and the value of annual mean is 83.4 Wm^{-2} .

Fig. 33 shows spatial distribution of monthly mean sensible heat flux radiation in the study area (1988 to 2000). Sensible heat flux appeared more greatly to fall (October) and in winter (January) than in summer (July). The spatial distribution characteristics of the YS, the ECS and the ES show more clearly in winter. The sensible heat flux in summer season is near to 0 or has negative values. This means in the summer that atmosphere provides heat in sea, but magnitude of the flux value is very smaller than in winter. On the other hand, in the winter shows value more than about 120 Wm^{-2} . Because sensible heat flux is value that depend on wind speed and temperature difference except given coefficient (ρ and C_P). Wind speed is stronger in winter than in summer season and sensible heat flux is higher in winter season than in the summer season. In the

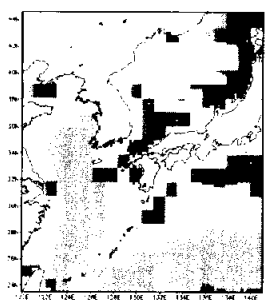
case of estimation of the sensible heat flux by bulk aerodynamics method, the sensible heat flux is influenced according to wind speed and temperature difference. It is bigger in winter that wind speed and temperature difference are large. In this study area, the sensible heat flux shows large at the ES. Sensible heat flux for each area is 27.6 Wm^{-2} , 31.3 Wm^{-2} , and 32.4 Wm^{-2} , respectively. The wind speed appeared as is small because sea level temperature adapts fast relatively about temperature change at the YS's occasion that anxiety is smaller than other area and temperature difference is small. Because the YS adapts fast sea surface temperature relatively to temperature change.



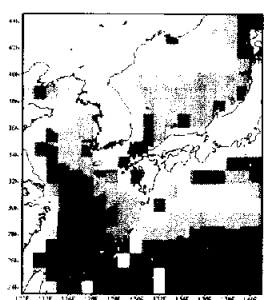
(a) January



(b) February

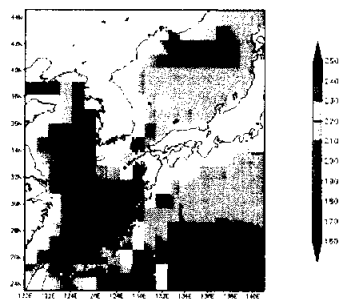


(c) March

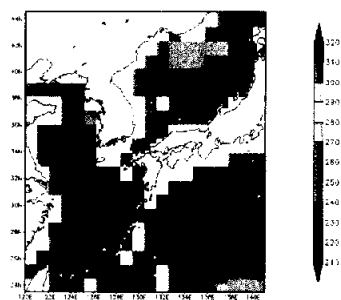


(d) April

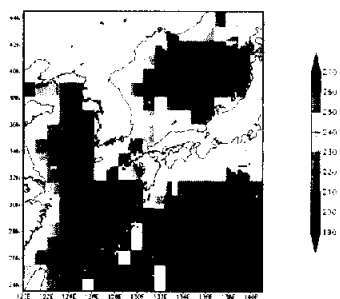
Fig. 29. Spatial distribution of the 13 years (1988 to 2000) monthly of net heat flux (in W/m^2). Negative value indicates the heat flux upward from the sea to the atmosphere.



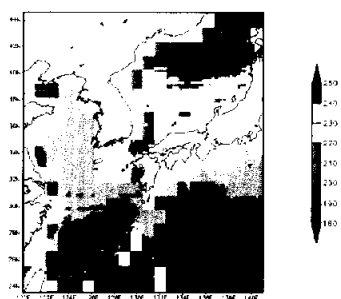
(e) May



(f) June

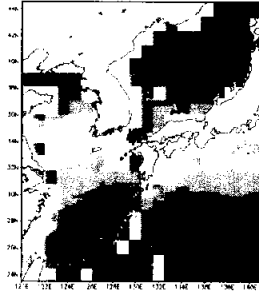


(g) July

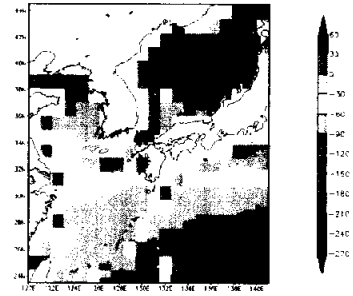


(h) August

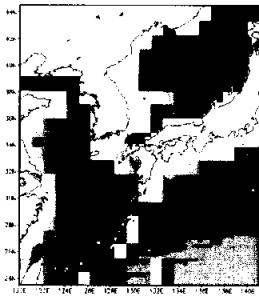
Fig. 29. (continued).



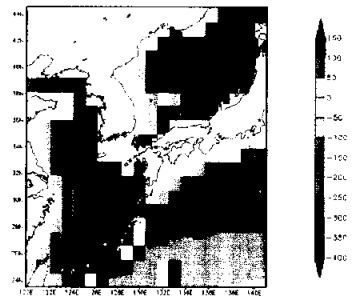
(i) September



(j) October

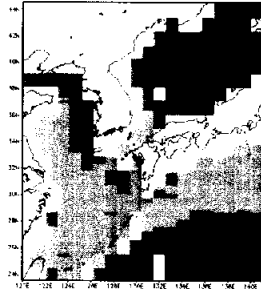


(k) November

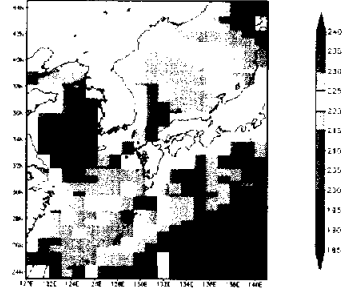


(l) December

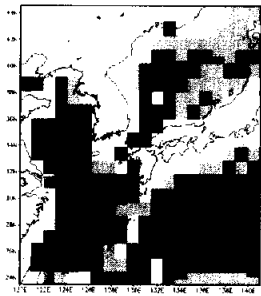
Fig. 29. (continued).



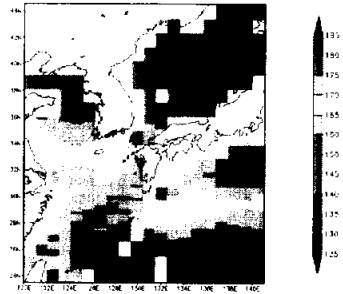
(a) January



(b) April

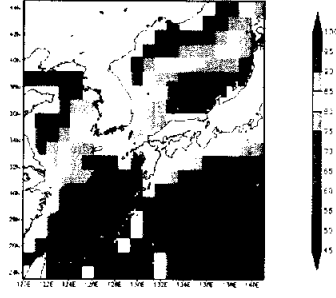


(c) July

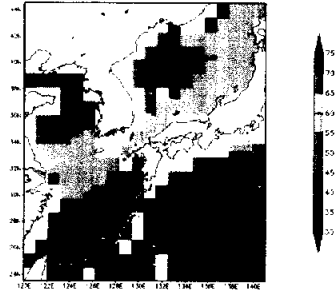


(d) October

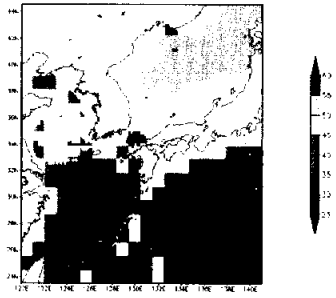
Fig. 30. Monthly mean shortwave radiation flux, Q_s in W/m^2 (1988 to 2000).



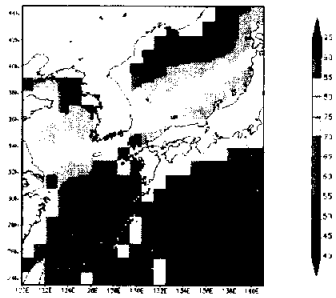
(a) January



(b) April

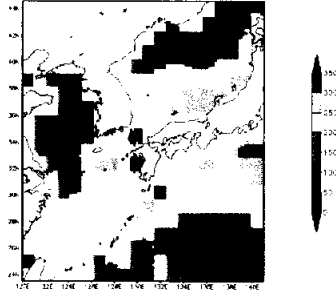


(c) July

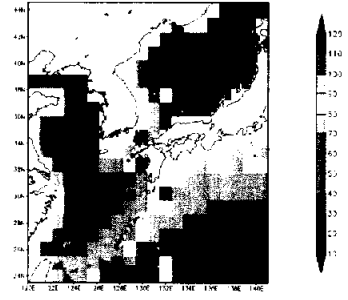


(d) October

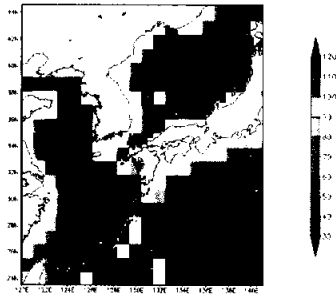
Fig. 31. Monthly mean longwave radiation, Q_L in W/m^2 (1988 to 2000).



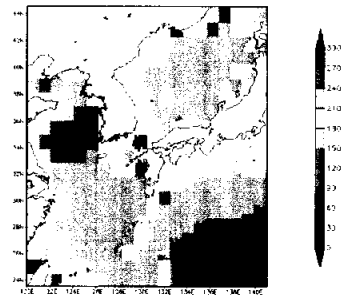
(a) January



(b) April

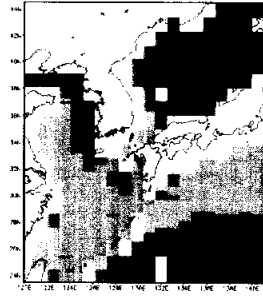


(c) July

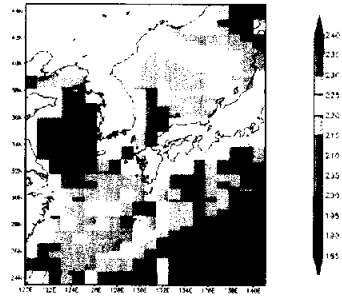


(d) October

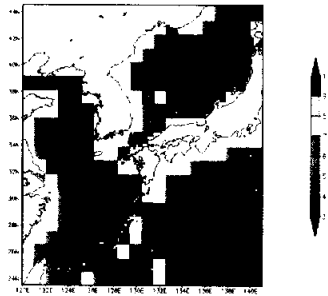
Fig. 32. Monthly mean latent heat flux, Q_E in W/m^2 (1988 to 2000).



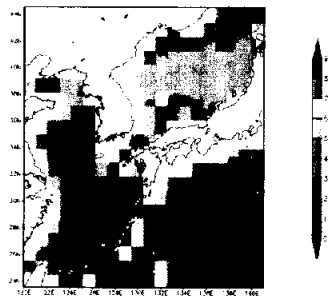
(a) January



(b) April



(c) July



(d) October

Fig. 33. Monthly mean sensible heat flux, Q_H in W/m^2 (1988 to 2000).

The 13-year mean seasonal variation of the monthly mean fluxes (net heat flux, shortwave radiation, longwave radiation, sensible heat and latent heat flux) at the YS is shown in Fig. 34. The shortwave radiation flux shows minimum value in winter (December) and is beginning to increase gradually in 96 Wm^{-2} in January and has maximum value (263 Wm^{-2}) in June and holds value of 250 Wm^{-2} until August. The maximum value is not showed in July that represent the summer season and showed in June. This causes through disturbance of shortwave radiation by cloud due to cyclogenesis of rainy season. The maximum value (77 Wm^{-2}) of longwave radiation showed in the winter season and minimum value (20 to 30 Wm^{-2}) showed in August by cloud distribution in summer season. The sensible heat flux is decided by strength of wind speed and temperature difference and appeared more than maximum 200 Wm^{-2} in winter. Variations of latent heat flux appeared maximum value in the winter season (120 to 180 Wm^{-2}) and minimum value (22 Wm^{-2}) in July. Therefore, aspect that absorb heat from atmosphere entering in April emitting heat into atmosphere by maximum -230 Wm^{-2} at December and January because net heat flux less than (100 Wm^{-2}) begins to appear in October if change of net heat flux that extracted longwave radiation flux. It is beginning to absorb heat by value more than 240 Wm^{-2} entering in June and heat emits at autumn season. Such aspect becomes unstable gradually because air mass is supplied heat and vapor passing from

West to East sea in winter season and strength of wind speed and distribution of cloud appeared extremely. The annual mean heat balance distribution of the YS has 175 Wm^{-2} for net heat flux. Longwave radiation flux is 54 Wm^{-2} , sensible heat flux is 28 Wm^{-2} , latent heat flux appeared by 85 Wm^{-2} .

The 13-year mean seasonal variation of the monthly mean fluxes (net heat flux, shortwave radiation, longwave radiation, sensible and latent heat flux) at the ECS was shown in Fig. 35. The solar radiation is larger south area than north area of study area if consider latitudinal diurnal change from top of atmosphere. However, solar radiation is larger at the ECS between April and June. This is caused in variations of cloudiness. As a result, the ECS receives maximum of solar radiation flux at June and July. The annual mean of shortwave radiation flux at the ECS was about 188 Wm^{-2} . The longwave radiation flux is shown small spatial variations through whole and changes to about 20 to 70 Wm^{-2} . The annual mean of the longwave radiation flux is about 50 Wm^{-2} at the ECS. The long term monthly variations of the sensible heat and latent heat flux are small variations and magnitude in the summer season and was getting bigger in the autumn and showed maximum in winter. The annual mean of the sensible heat and latent heat flux at the ECS are 30 Wm^{-2} and 105 Wm^{-2} , respectively.

The 13-year mean seasonal variations of the monthly mean fluxes (net heat flux, shortwave radiation, longwave radiation, sensible and

latent heat flux) over the ES is shown in Fig. 36. The annual mean of the net heat flux, sensible and latent heat flux at the ES are 70 Wm^{-2} , 32 Wm^{-2} and 108 Wm^{-2} , respectively. The mean shortwave radiation flux at the ES shows maximum (272 Wm^{-2}) in July, and this is because cloudiness is the smallest in July. Also, the annual mean distribution of the shortwave radiation flux at the ES shows more greatly in the Continent than in the Sea, because this is formation of vigorous convection and cloud in sea (Husing, 1986; Kim, 1992). The longwave radiation flux shows as the variation is small extending all year. The monthly mean variations that treat in sensible heat and latent heat flux in summer is small in magnitude and spatial volatility almost be. The latent heat flux begun to great in September and showed maximum (191 Wm^{-2}) in January. Net heat flux is value of a positive from March to September and displayed value of negative from October to February. These variations agree well in maximum and minimum of sea surface temperature from March to September. Table 10 is statistical values for heat fluxes at the each area. On the whole, the ECS and the ES showed larger than the YS for all heat fluxes components.

To compare these results with previous research, compared results that obtained around the ES. Table 11 is the seasonal and annual mean values of the sensible heat and latent heat flux at the ES estimated by the previous and present studies. All studies used bulk coefficient (C_H , C_E) that is proposed by Kondo (1975). Kondo *et al.*,

(1994) put assumption of neutral condition and calculated turbulent heat flux. As a result, the values was small relatively. The results of Kato and Asai (1983), Kim (1992) and present study are larger than them of Park *et al.* (1995) and Hirose *et al.* (1996) in winter. This result considers that is caused in difference of used data.

Table 10. The monthly mean values of heat fluxes at the each area.

The YS, the ECS and the ES mean the Yellow Sea, the East China Sea and the East Sea. Unit is Wm^{-2} .

(a) Net heat flux (Q_N)

Month	YS	ECS	ES
1	-217.4	-197.3	-198.2
2	-142.1	-134.0	-135.4
3	1.65	10.9	11.3
4	172.1	186.5	187.9
5	218.8	231.3	233.3
6	246.1	250.0	250.0
7	238.3	251.0	251.6
8	218.5	230.7	232.1
9	157.9	176.3	178.5
10	73.7	50.2	-49.0
11	-168.1	-126.0	-126.4
12	-236.6	-192.9	-194.5
mean	34.6	53.1	53.4

(b) Shortwave radiation flux (Q_S)

Month	YS	ECS	ES
1	96.3	107.3	108.8
2	134.5	142.6	143.9
3	175.8	180.4	181.8
4	217.7	222.5	223.7
5	249.0	253.0	254.2
6	263.1	263.0	263.7
7	261.7	271.3	272.5
8	236.9	247.9	249.3
9	195.4	207.4	209.0
10	147.5	162.0	163.6
11	102.3	113.7	117.6
12	85.2	96.6	99.8
mean	180.5	189.0	190.7

(c) Longwave radiation flux (Q_B)

Month	YS	ECS	ES
1	70.9	69.9	70.3
2	77.0	76.2	76.7
3	77.4	76.6	77.3
4	50.6	51.6	52.4
5	48.4	50.1	50.9
6	42.3	42.3	43.0
7	31.6	34.2	35.1
8	22.7	26.7	27.5
9	30.1	32.6	32.0
10	65.3	63.0	63.2
11	66.6	61.8	63.6
12	66.8	63.4	65.1
mean	54.1	54.0	54.8

(d) Sensible heat flux (Q_H)

Month	YS	ECS	ES
1	89.5	83.8	84.6
2	84.3	82.3	83.6
3	42.6	46.6	47.8
4	-9.4	-1.4	-0.1
5	-10.4	-2.3	-1.1
6	-10.8	-1.9	-0.6
7	9.8	-1.4	-0.2
8	9.7	-1.2	0.1
9	12.3	20.8	22.2
10	28.8	34.2	35.4
11	49.0	48.6	49.1
12	74.5	67.9	68.0
mean	27.6	31.3	32.4

(c) Latent heat flux (Q_E)

Month	YS	ECS	ES
1	147.6	184.7	191.5
2	120.0	159.7	166.0
3	65.4	95.2	98.7
4	26.2	41.7	43.9
5	22.9	36.1	37.7
6	22.8	44.3	46.6
7	36.3	47.3	49.0
8	33.9	46.6	48.6
9	95.4	115.0	117.9
10	125.8	144.6	148.1
11	150.0	164.5	167.3
12	176.8	184.3	188.4
mean	83.4	105.3	108.6

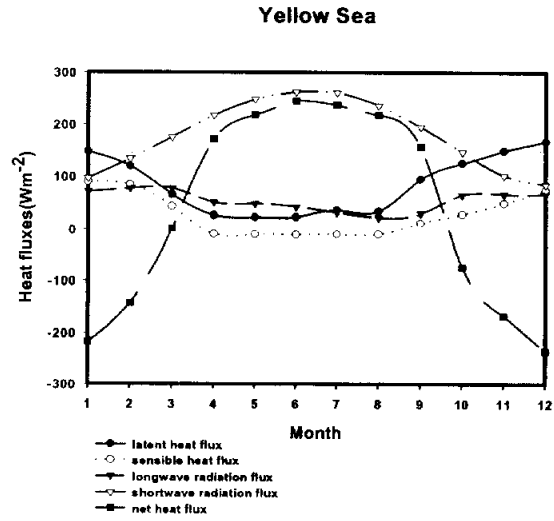


Fig. 34. The 13-year mean seasonal variation of the monthly mean fluxes over the YS.

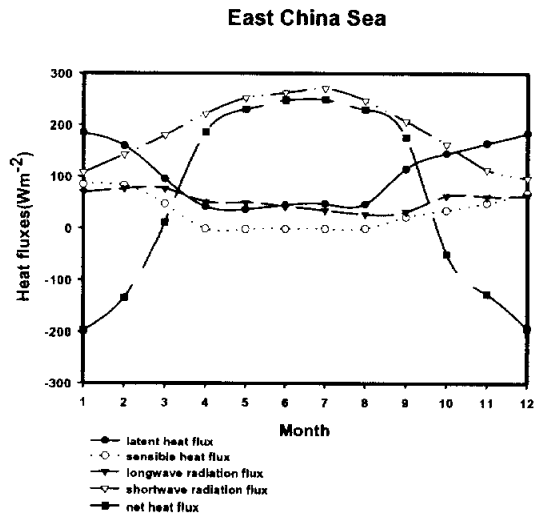


Fig. 35. Same as Fig. 34. but for ECS.

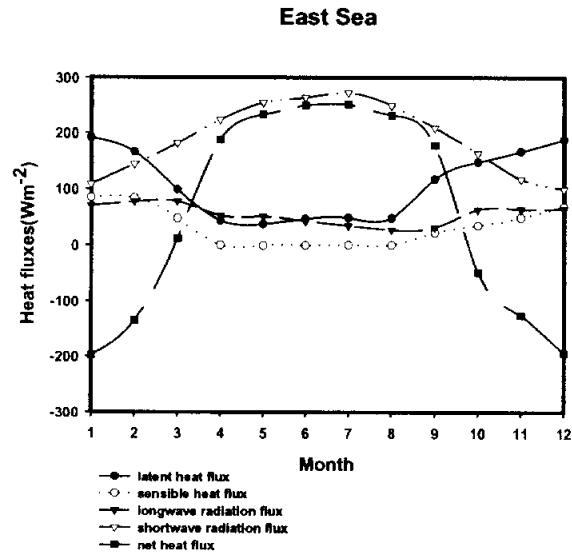


Fig. 36. Same as Fig. 34. but for ES.

Table 11. The seasonal and annual mean values of the sensible and latent heat flux at the East Sea estimated by the previous and present studies. The 'spr.' is defined as the three months from March to May.

	Kato (1981,83)	Kim (1992)	Kondo (1994)	Park <i>et al.</i> (1995)	Hirose <i>et al.</i> (1996)	Present study
period	1978-79	1962-86	1965-90	1961-90	1960-90	1988-2000
resolution	2° × 2°	2° × 2°	1° × 1°	0.2°×0.2°	1° × 1°	1° × 1°
n						
Q _h spr.	12	17	5	8	9	15
Q _h sum.	-5	2	-5	-2	-1	-0.5
Q _h aut.	48	55	33	25	42	36
Q _h win.	132	137	88	97	108	79
Q _h ann.	47	53	31	32	40	32
Q _e spr.	57	47	38	43	46	60
Q _e sum.	29	32	26	17	35	48
Q _e aut.	153	144	124	138	147	144
Q _e win.	169	180	123	161	143	180
Q _e ann.	102	101	78	90	93	108

5.2.2 Annual variations

In this section analyzed annual variations characteristics of heat fluxes (sensible and latent heat flux, longwave and shortwave radiation flux, net heat flux) using long term data (1988 to 2000).

Fig. 37 shows annual variations of the sensible heat flux at the YS, the ECS and the ES. Because value of sensible heat flux show clearly in summer and in winter over all areas, the lower part was shown some horizontal segment in figure, this part is corresponding in summer (about 0 Wm^{-2}). During analysis period, sensible heat flux was the highest in winter, 1996.

Annual variations of the latent heat flux at the YS, the ECS and the ES was shown in Fig. 38. Inclination of variations showed similarly whole year in all areas and latent heat flux showed larger at the ES than the YS and the ECS through whole year. Latent heat flux was the highest during analysis period appeared at the ES in winter, 1992.

Fig. 39 to 41 show annual variations of the longwave radiation, shortwave radiation and net heat flux at the YS, the ECS and the ES, respectively. Firstly, the longwave radiation variations that is whole during analysis period in three areas all showed similar tendency and the value was large at the YS on the whole. Reason that the longwave radiation flux showed large like this at the YS can find in cloudiness and temperature difference that affected in the

longwave radiation flux as referred before. This is the reason why, because temperature difference was large at the YS, and was smaller than other areas (the ECS and the ES) that differ cloudiness. the longwave radiation flux showed more greatly. Secondly, the annual variations of the shortwave radiation flux displayed same value in all of the three areas over all year. The lowest value is in 1992 and 1996 during analysis period, and the value showed about 50 Wm^{-2} . This can explain relating with cloudiness. Because cloudiness value appeared more than annual mean 0.6 at the ES in 1992 and 1996.

Net heat flux also showed similarly tendency in all of the three areas. The area that is shown minimum value in study area is at the YS and appeared about -300 Wm^{-2} in 1991 and 1992.

Sensible heat and latent heat flux showed clearly difference in annual variations as well as seasonal variations. Convection in the ocean is dominated by sensible heat and latent heat flux and these fluxes depends on the dynamic effect (wind speed) and thermal effect (sea surface temperature and air temperature or sea surface specific humidity or specific humidity over the sea). Therefore, it was compared each term relative magnitude estimating by differential of Eqs. (3.17) and (3.18) to compare change of wind speed, temperature difference and specific humidity difference that influenced sensible heat and latent heat flux in sea level.

$$\frac{\partial Q_H}{\partial t} = \rho C_P C_H \frac{\partial \overline{U_{10}}}{\partial t} (\overline{T_s - T_a}) + \rho C_P C_H \overline{U_{10}} \frac{\partial}{\partial t} (\overline{T_s - T_a}) \quad (5.1)$$

I

II

III

$$\frac{\partial Q_E}{\partial t} = \rho L_v C_E \frac{\partial \overline{U_{10}}}{\partial t} (\overline{q_s - q_a}) + \rho L_v C_E \overline{U_{10}} \frac{\partial}{\partial t} (\overline{q_s - q_a}) \quad (5.2)$$

where Term I represents differential of the sensible heat and latent heat flux in the ocean. Term II represents time variations of the wind speed, that is, dynamic effect. Term III represents time variations of the temperature and specific humidity difference, that is, thermal effect. At this time, air density and heat transfer coefficient (C_H and C_E) supposed that is fixed. Results that examine separating change by time of sensible heat and latent heat flux by two terms (dynamic effect and thermal effect) in sea level appeared from Fig. 42 to Fig. 47.

Annual variations of dynamic effect and thermal effect for sensible heat flux at the YS, the ECS and the ES was shown from Fig. 42 to Fig. 44. In case of summer season, time variations of all areas was hardly seen, this is not meaning that dynamic effect and thermal effect is zero, but variations of wind speed and sea surface temperature difference between two periods are meaning that is not. Term II (dynamic effect) in winter season appeared more predominately than term III (thermal effect). Time variation of the thermal effect means more greatly effect on the sensible heat flux

than that of dynamic effect. Also, term II and term III in spring season effect on decreasing for sensible heat flux and the thermal effect showed more greatly than dynamic effect.

Annual variations of dynamic effect and thermal effect for latent heat flux at the YS, the ECS and the ES was shown from Fig. 45 to Fig. 47. Unlike sensible heat flux, in case of dynamic effect of latent heat flux showed more greatly than thermal effect in summer season. In winter season, thermal effect and dynamic effect all it causes an effect in change of latent heat flux. Also, in case of dynamic effect of latent heat flux showed more greatly than thermal effect in spring season. As a results, the sensible and latent heat flux due to the variation are dynamic effect compared with the fact that it causes the effect where the variation due to thermal effect is larger. Fig. 48 shows time series of annual mean fluxes at the YS, the ECS and ES. Sensible heat flux, latent heat flux and net heat flux are displaying annual variations of sinusoidal function and longwave and shortwave radiation flux displayed almost regular shape.

5.2.3 Case study

In this section, when there is change of sea surface temperature, we analyzed changing pattern of sensible heat and latent heat flux. In analysis period selected in January, 1995 that occurs rising of the sea surface temperature in winter among research periods (1988 to 2000).

Fig. 49 showed monthly mean time series of sea surface temperature between 1994 and 1996. The 1995 in winter (January to March) can see that sea surface temperature was increasing about $2^{\circ}\text{C} \sim 6^{\circ}\text{C}$ than ordinary year. This phenomena analyzed through horizontal section of area A and A' of Fig. 50. A and A' area were area that horizontal gradient change of sea surface temperature is the most clearly.

Fig. 51 displays horizontal gradient of sea surface temperature with latitude for A and A' area. Fig. 51 (a) and 51 (c) showed horizontal gradient of sea surface temperature in January, 1994 and 1996. The magnitude of horizontal gradient could know which horizontal gradient was clearly as high latitude to low latitude. However, due to rise of sea surface temperature in January, 1995, it could know that horizontal gradient of sea surface temperature was dwindled rapidly.

Fig. 52 shows time series of sea surface temperature with latitude during analysis period. The 1995 in January was confirmed that

rising of whole sea surface temperature than in 1994 and 1996, and horizontal gradient was also dwindled rapidly with latitude. Fig. 53 shows wind speed with latitude. Horizontal gradient of sea surface temperature could know that wind speed was reduced on January, 1995. This is directly cause that sensible heat flux was decreased in Fig. 54.

Fig. 55 displays change of latent heat flux with latitude. Despite wind speed decreased, it was almost fixed with latitude in case of latent heat flux. This is that specific humidity over sea surface increased and appeared by increasing of latent heat flux finally according as sea surface temperature increased. Therefore, if sea surface temperature increased, sensible heat flux decreased and latent heat flux increased. Because magnitude of latent heat flux was big relatively while sensible heat flux decreased. Turbulent Kinetic Energy (TKE) becomes actively, and atmospheric circulation of synoptic scale was occurred.

5.3 Air-sea interaction and climate

Actually, the ocean is system that interaction with atmosphere is very excellent. It means that this effects easily impact of air-sea and also atmosphere can effect easily impact of sea. For example, if solar radiation energy which sea goes changes by particulate matter, volcano explosion, fine sand particle of desert etc., heat exchange of air-sea are changed immediately. This is some of weather change and cause climate fluctuation in a long-term standpoint. If is connected with direction that this control action is not desirable or any reason, it is connected by environment change of global scale and human by this of course, effect that shudder in all creature ecosystems anyone to direction that hard to predict.

The earth is situated in interaction of air-sea, and the human is living pacifically by balance of this harmonious nature. But, this equilibrium by human's activity was placed in crisis to be broken present. To overcome this crisis, study of the latest sea and atmosphere environment is proceeded very vigorously. Atmosphere and sea are exchange to dynamic and thermodynamic through sea surface boundary layer. The heat exchange process of atmosphere-sea interacts on important elements in meteorological phenomena of a global scale as well as local meteorological phenomena. The heat exchange of atmosphere-sea through sea surface cause convective activity of atmosphere, and atmosphere

causes flowing of sea surface by wind speed. Sea does it so that may transfer heat, vapor and energy that is flowed in from atmosphere into sea inside and causes variations of ocean circulation. Internal energy of sea causes direct effect in that emit into atmosphere in form of heat fluxes to atmospheric circulation and convection. Therefore, interaction attained through boundary layer of atmosphere and sea will be very important to dynamic mechanism.

Weather and climate of our country that surrounded by the sea are effecting fairly much impact by the ocean. The release of the sensible heat and latent heat flux connected with synoptic scale weather system supply to water vapor and instabilize and cause a lot of rains and snows in seaside district by local circulation. Also, huge phenomenon called Elnino exists as for global scale. Therefore, because to analyze air-sea interaction to use remote sensing is useful to climate change watch as well as weather change watch of global scale, the research of air-sea interaction can supply still more better information to examine closely cause getting by climate system.

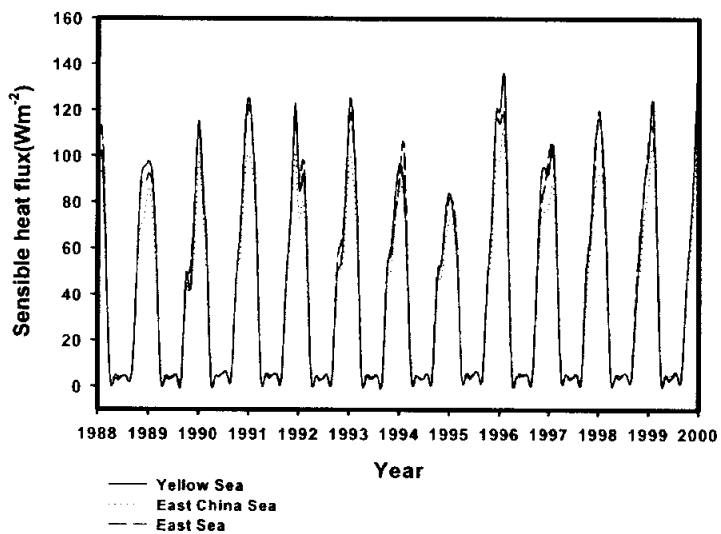


Fig. 37. Annual variations of the sensible heat flux.

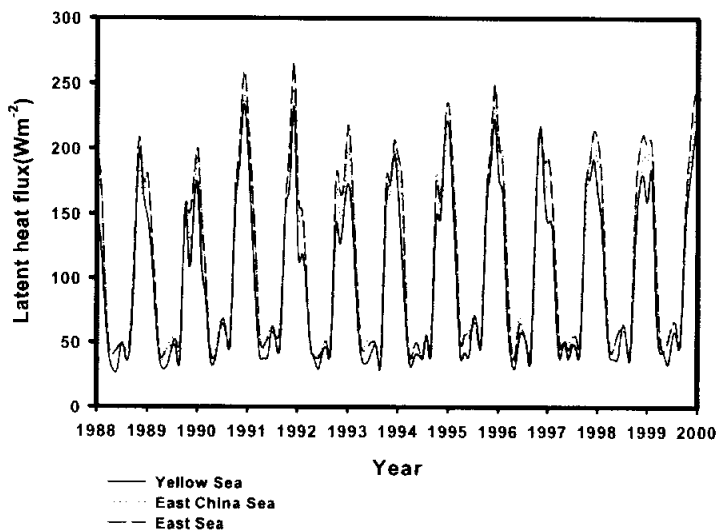


Fig. 38. Same as Fig. 37. but for latent heat flux.

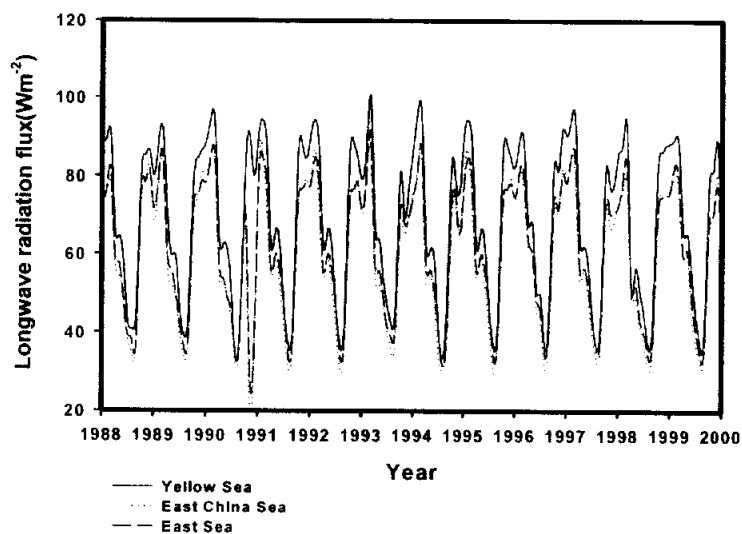


Fig. 39. Same as Fig. 37. but for longwave radiation flux.

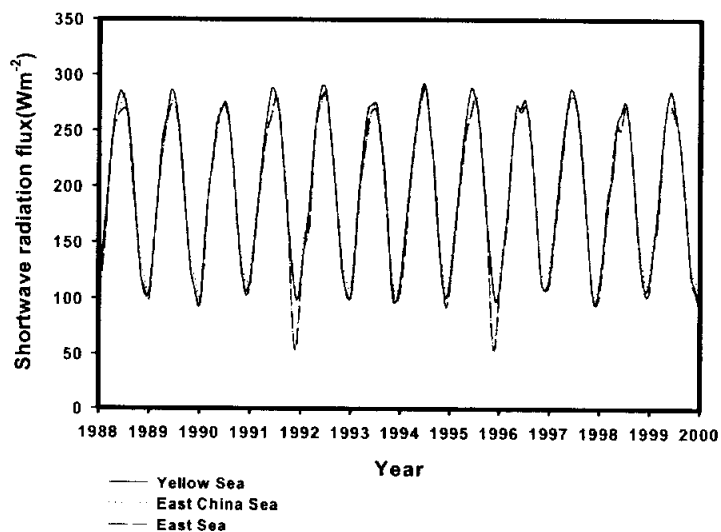


Fig. 40. Same as Fig. 37. but for shortwave radiation flux.

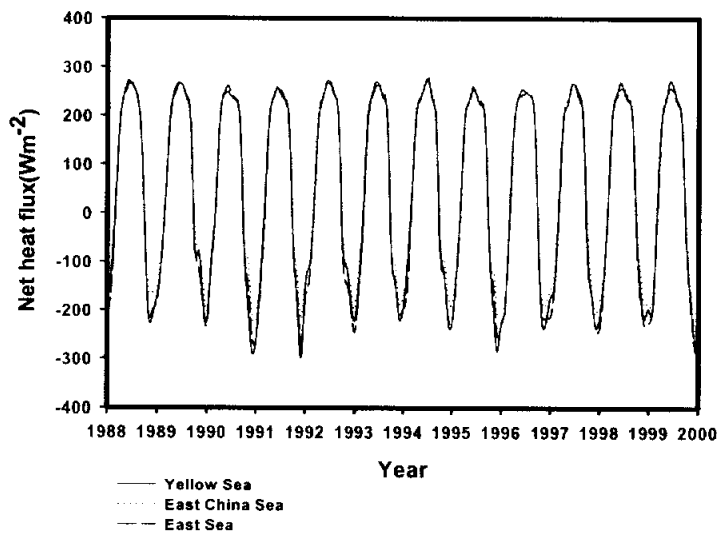


Fig. 41. Same as Fig. 37 but for net heat flux.

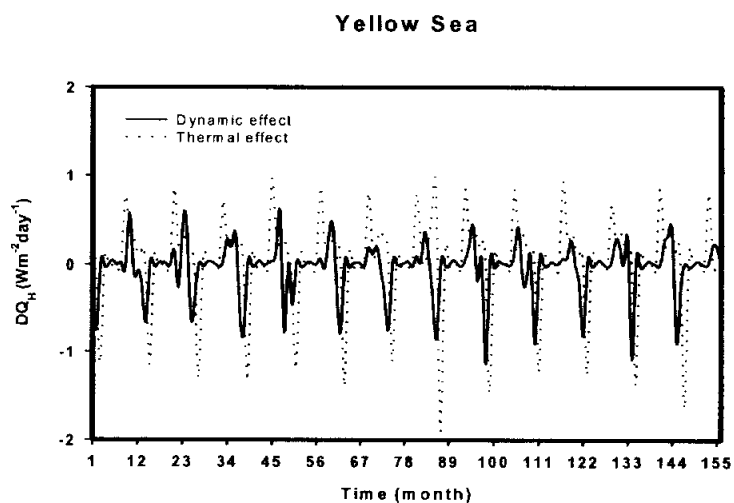


Fig. 42. Comparison of dynamic and thermal effect for sensible heat flux at the YS (1988 to 2000).

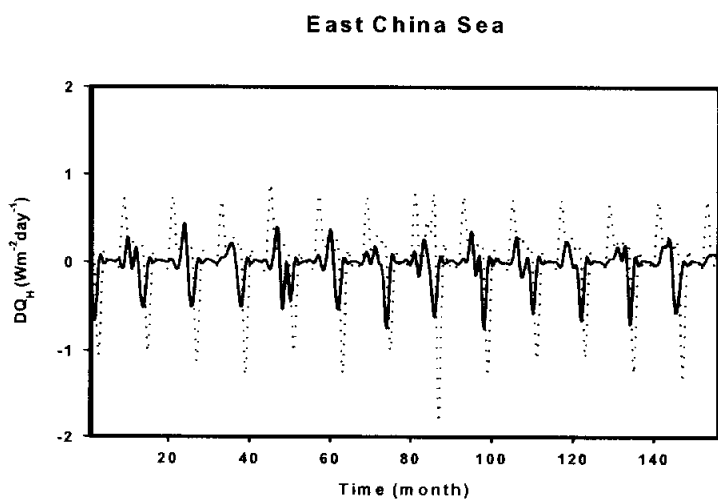


Fig. 43. Same as Fig. 42. but for ECS.

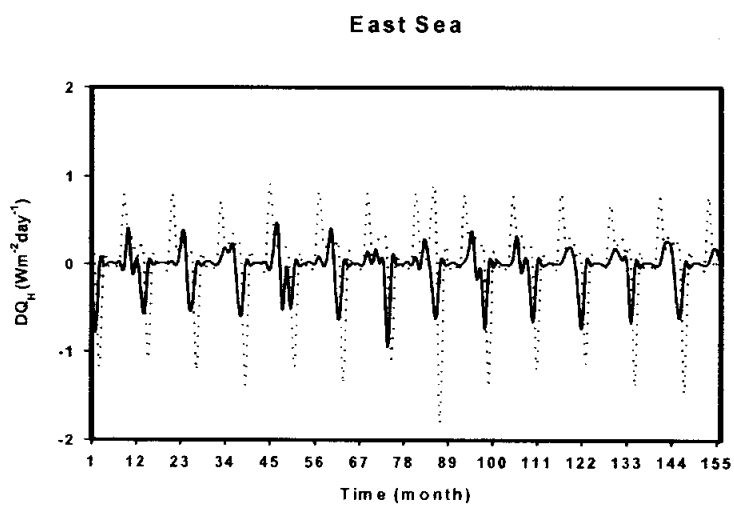


Fig. 44. Same as Fig. 42. but for ES.

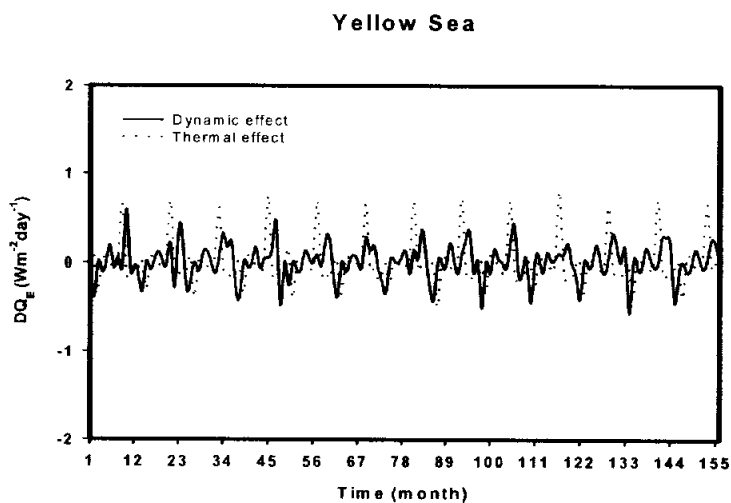


Fig. 45. Comparison of dynamic and thermal effect for latent heat flux at the YS (1988 to 2000).

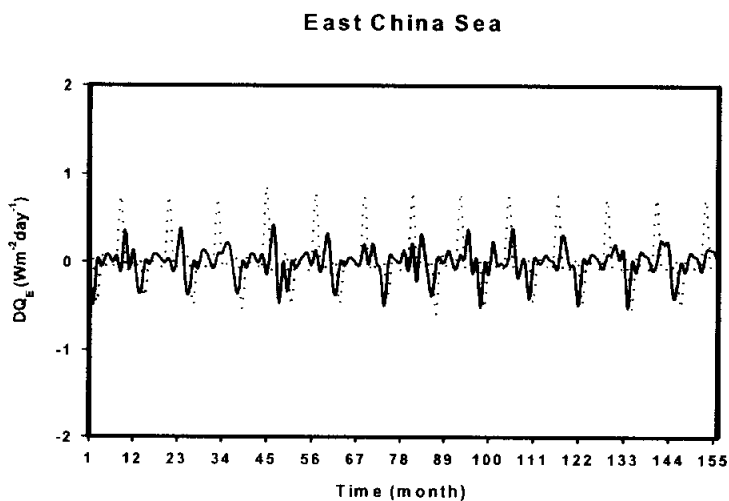


Fig. 46. Same as Fig. 45. but for ECS.

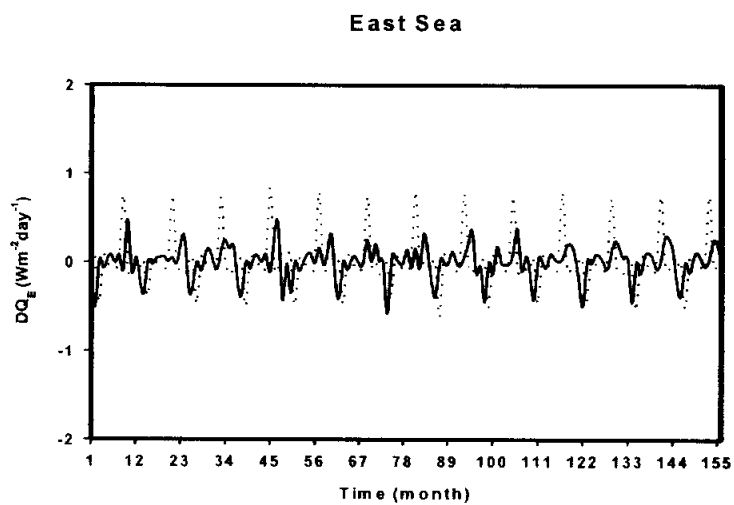
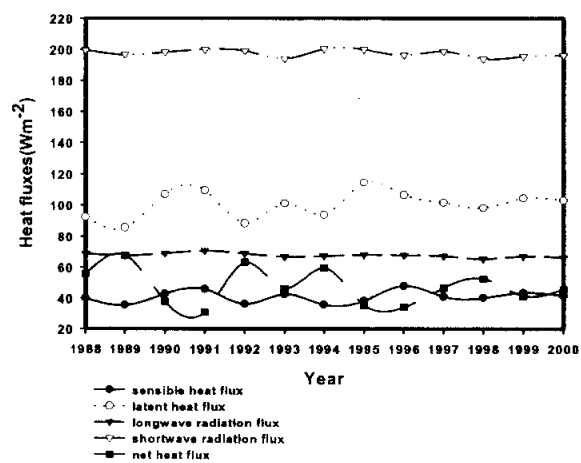
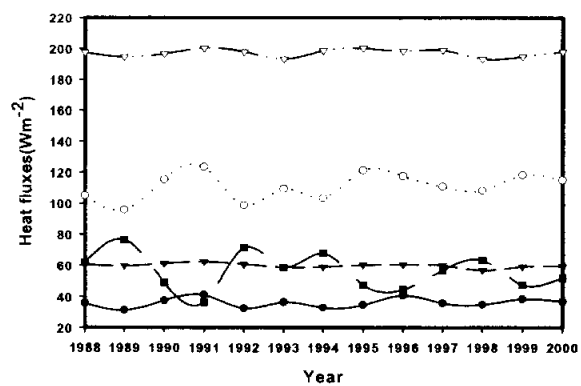


Fig. 47. Same as Fig. 45. but for ES.

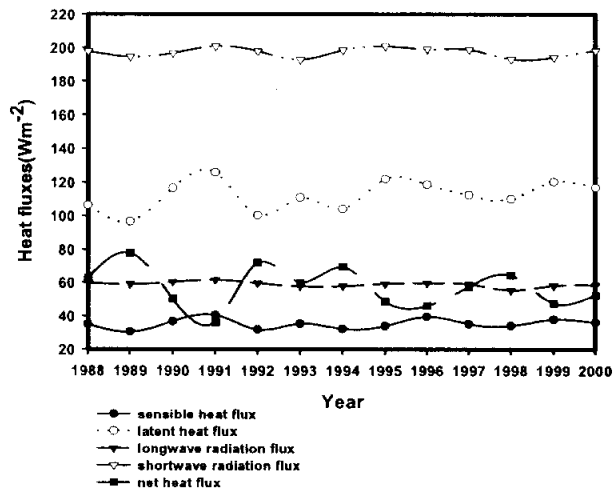


(a) YS



(b) ECS

Fig. 48. Annual mean fluxes at the YS (a), ECS (b), and the ES (c).



(c) ES

Fig. 48. (continued).

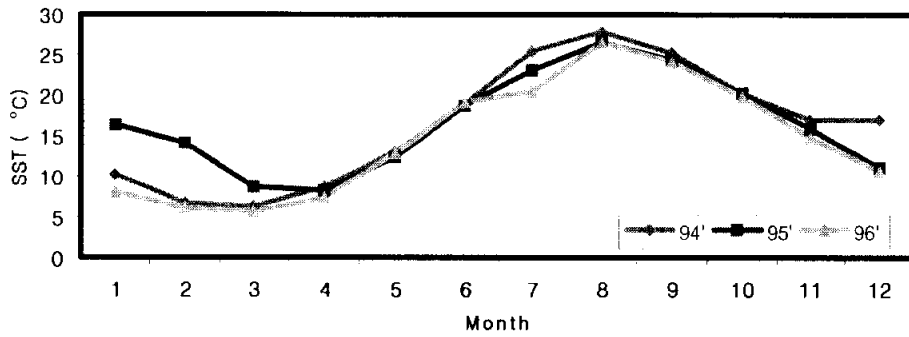


Fig. 49. Time series of monthly SST between 1994 and 1996.

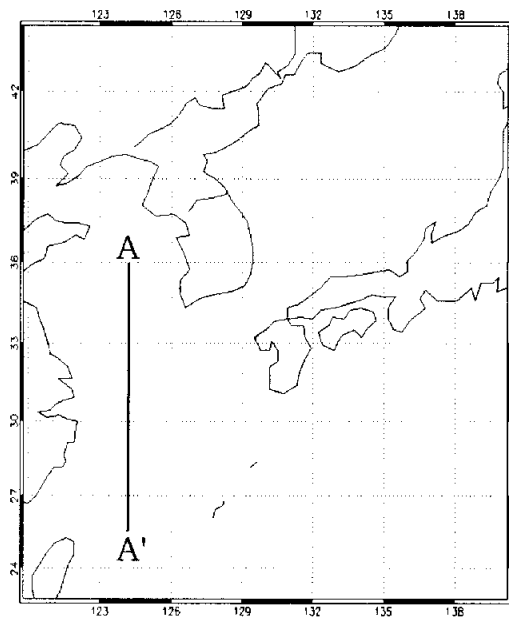
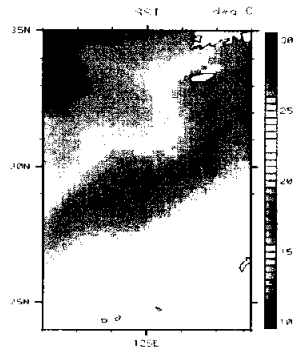
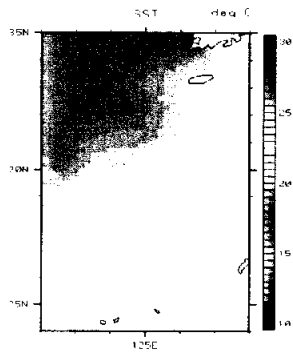


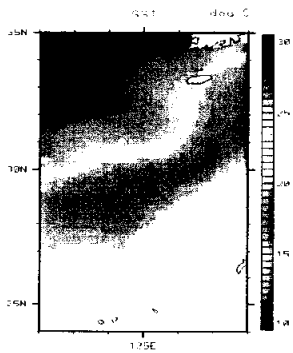
Fig. 50. Horizontal cross section of A to A' area for case study area



(a) January, 1994



(b) January, 1995



(c) January, 1996

Fig. 51. Horizontal cross section of A and A' by NOAA MCSST.

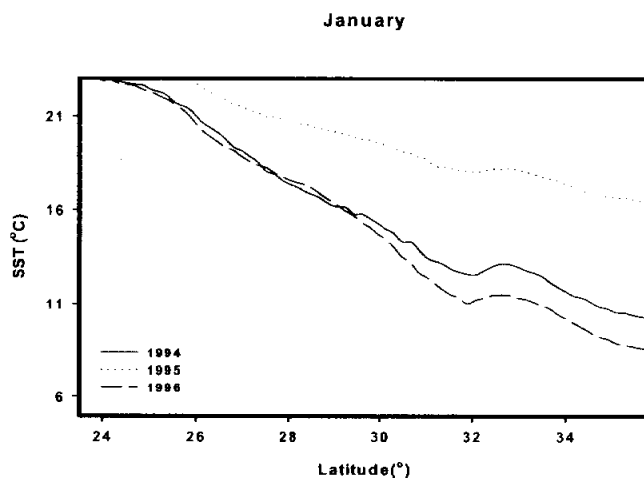


Fig. 52. Variation of SST with latitude in January.

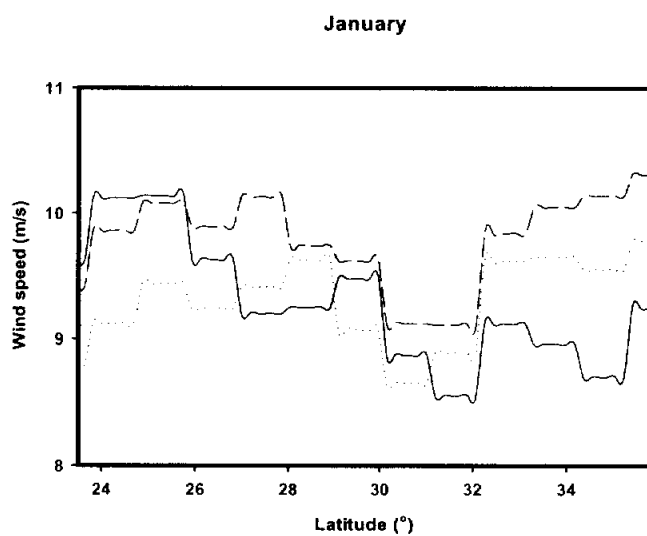


Fig. 53. Variation of wind speed with latitude in January.

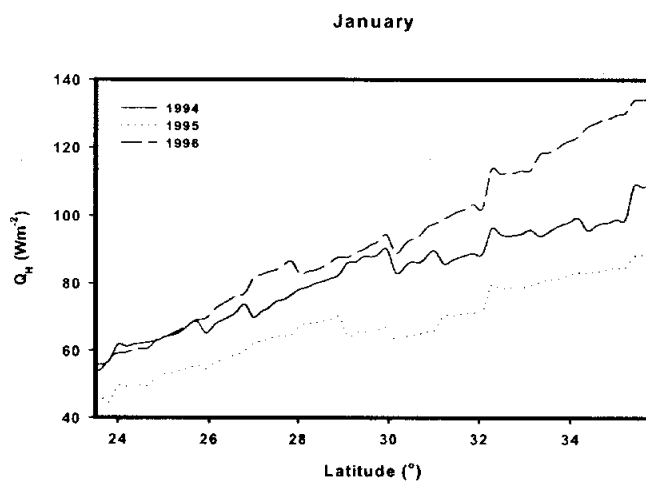


Fig. 54. Variation of sensible heat flux with latitude in January.

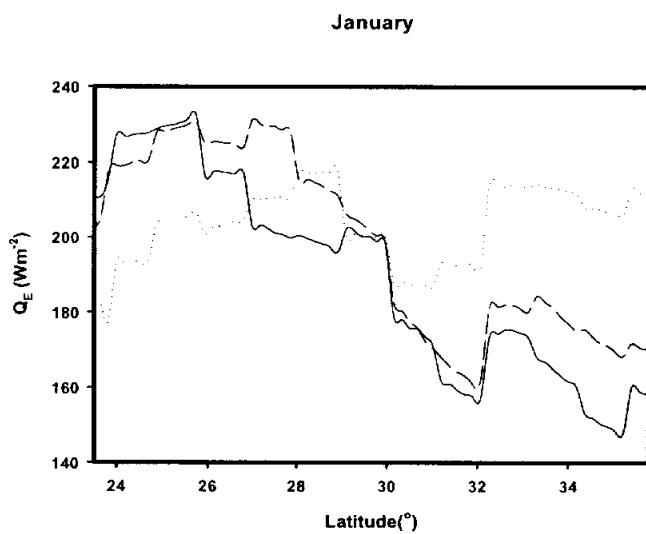


Fig. 55. Variation of latent heat flux with latitude in January.

VI. Turbulent kinetic energy (TKE)

Turbulent kinetic energy (called TKE hereafter) which is a measure of the intensity of turbulence is one of the most important variables in micrometeorology, it is directly related to the momentum, heat and moisture transport through the boundary layer. TKE is also sometimes used as a starting point for approximations of turbulent diffusion.

The individual terms in the TKE budget equation describe physical processes that generate turbulence. The relative balance of these processes determines the ability of the flow to maintain turbulence or become turbulent, and thus indicates flow stability. Some important dimensionless groups and scaling parameters are also based on terms in the TKE equation.

The definition of TKE is $\text{TKE}/m = \bar{e} = 0.5(\overline{u'^2} + \overline{v'^2} + \overline{w'^2})$. TKE/m is nothing more than the summed velocity variances divided by two. Therefore, starting with the prognostic equation for the sum of velocity variances and dividing by two easily gives the TKE budget equation:

$$\begin{aligned}
\frac{\partial \bar{e}}{\partial t} = & \underbrace{-\overline{u'w'} \frac{\partial \bar{u}}{\partial z}}_{\text{II}} - \underbrace{\overline{v'w'} \frac{\partial \bar{v}}{\partial z}}_{\text{III}} - \underbrace{\frac{\partial (\overline{w'e'})}}_{\text{IV}} - \underbrace{\frac{1}{\rho} \frac{\partial (\overline{w'p'})}}_{\text{V}} \\
& + \underbrace{\frac{g}{T} [\overline{(w'\theta')} + 0.61 T \overline{(w'q')}] - \epsilon}_{\text{VI}}. \quad (6.1)
\end{aligned}$$

Term I represents local storage or tendency of TKE. Term II describes the advection of TKE by the mean wind. Term III is the buoyant production of consumption term. It is a production or loss term depending on whether the heat flux is positive or negative. Term IV is a mechanical or shear production/loss term. The momentum of the wind is usually lost downward to the ground. Thus, Term IV results in a positive contribution to TKE when multiplied by a negative sign. Term V represents the turbulent transport of TKE. Term VI is pressure correlation term that describes how TKE is redistributed by pressure perturbations. Term VII represents the viscous dissipation of TKE; i.e., the conversion of TKE into heat. Turbulence is dissipative. Term VII is a loss term that always exists whenever TKE is non-zero. Physically, this means that turbulence will tend to decrease and disappear with time, unless it can be generated locally or transported in by mean, turbulent, or pressure process. Thus, TKE is not a conserved quantity (Stull, 1995).

Considering the wind direction along the average wind and

neglecting relatively small term,

$$-\overline{(u'w')} \frac{\partial \bar{u}}{\partial z} + \frac{g}{T} [\overline{(w'\theta')} + 0.61 T \overline{(w'q')}] - \epsilon = 0. \quad (6.2)$$

In the surface layer where the flux is constant, we can substitute $\overline{(u'w')}$ for u_*^2 . If the condition is close to neutral,

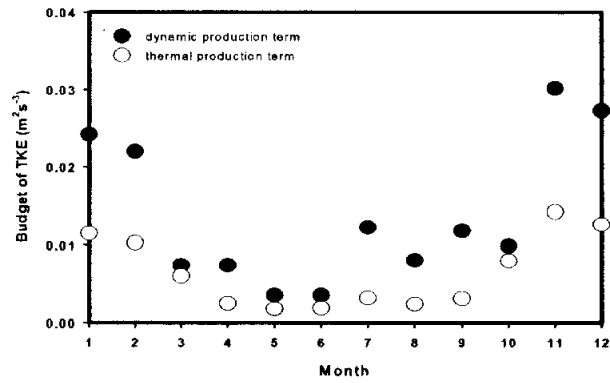
$$\frac{\partial \bar{u}}{\partial z} = \frac{u_*}{kz} \psi_m(z/L) \simeq \frac{u_*}{kz}, \quad (6.3)$$

$$-\frac{u_*^3}{kz} + \frac{g}{T} [\overline{(w'\theta')} + 0.61 T \overline{(w'q')}] - \epsilon = 0. \quad (6.4)$$

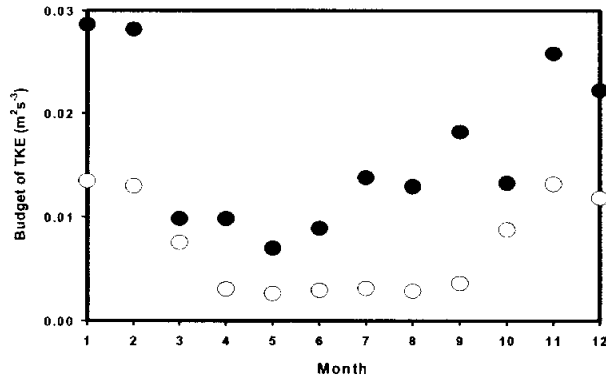
Turbulence refers to the apparently chaotic nature of many flows, which is manifested in the form of irregular, almost random fluctuations in velocity, temperature, and scalar concentrations around their mean value in time and space. The motions in the Atmospheric Boundary Layer (ABL) are almost always turbulent. In the surface layer, turbulence is more or less continuous. Turbulence is responsible for the efficient mixing and exchange of mass, heat and momentum throughout the ABL. In particular, the surface layer turbulence is responsible for exchanging these properties between the atmosphere and the sea surface. Without turbulence, such exchanges

would have been at the molecular scale and minuscule in magnitude. Mass exchange processes between the sea surface and the atmosphere, the radiation balance and the heat energy budget at or near the sea surface are also significantly affected. More direct effects of turbulent transfer on the surface heat energy budget are through sensible and latent heat exchanges between the sea surface and the atmosphere (Arya, 1988). The mechanism of Q_H and Q_E development can be analyzed from viewpoint of a turbulent kinetic energy.

Fig. 56 shows comparison of dynamic production term and thermal production term over the seas around the Korean Peninsula from TKE equation (6.4). Compared with the magnitude, the dynamic production is dominant throughout the year at the YS, the ECS and the ES (about 2 times as much as the thermal production term). Its value in summer season is a little small compared with that in winter season. This means that the Marine Atmospheric Boundary Layer (MABL) is far from the convective boundary layer in winter. The thermal production is about the same over the seas around the Korean Peninsula and dynamic production is more important in winter season than in summer season. Turbulence refers mainly to the wind which is a principal mechanism to transfer the heat from the all sides to the atmosphere. The surface layer become unstable by dynamic production during the winter season. It is noted that the production of TKE depends on the wind speed.

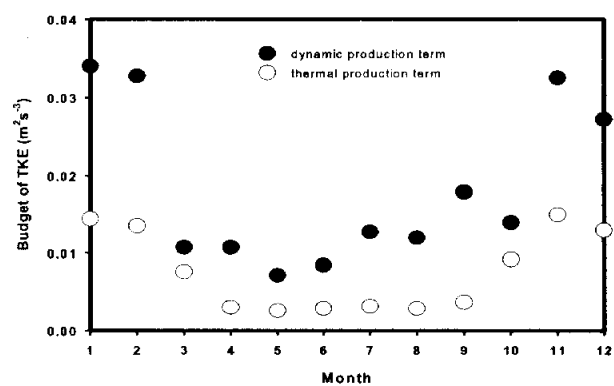


(a) YS



(b) ECS

Fig. 56. Comparison of dynamic production term and thermal production term over the seas around the Korean Peninsula.



(c) ES

Fig. 56. (continued).

VII. Conclusions

In this study, it is developed oceanic meteorological retrieval algorithm in order to understand mechanism of air-sea interaction using satellite data and buoy data and corrected to retrieval algorithm of the air-sea heat exchange. It is estimated and verified heat fluxes (sensible heat and latent heat flux, longwave radiation flux, shortwave radiation flux, net heat flux) using newly developed algorithm to the oceanic meteorological elements and air-sea heat exchange retrieval over the sea around the Korean Peninsula. Based on this process, it constructed oceanic meteorological elements display system that can display oceanic meteorological elements (sea surface temperature, sensible heat and latent heat flux, longwave radiation and shortwave radiation flux, and net heat flux) over the around the Korean Peninsula.

This study used a new method to obtain air temperature and sea surface specific humidity which cannot be directly observed by satellites. AT over sea surface is derived from the fourier series equation using only SST from satellite data. The derivation proved pretty satisfactory in terms of BIAS (0.28°C), RMSE (1.5°C) and correlative coefficient ($r=0.95$). Specific humidity is obtained from the non linear regression equation between vapor pressure (e_a) and AT from buoy data. It is then examined through comparisons both with

empirical equation from SSM/I suggested by Schlüssel *et al.*, (1995) and with newly developed equation. Both comparisons supported the obtained data in terms of BIAS (-1.42 g/kg) and RMSE (1.75 g/kg). Therefore these data with less than 10% error were good enough to be utilized in the derivation of surface heat flux over the sea.

Sensible heat flux appeared more greatly in fall and in winter than in summer. The spatial distribution characteristics of the YS, the ECS and the ES show more clearly in winter. The sensible heat flux in summer season is near to 0 or has negative values, this means in the summer that atmosphere provides heat in sea, but magnitude of the flux value is very small than winter.

Latent heat flux in the ocean appears maximum from autumn season to winter season. Maximum area of latent heat flux coincides almost with maximum area of specific humidity difference. Latent heat flux appeared greatly at the ECS, and appeared little at the YS over the sea around the Korean Peninsula.

Longwave radiation appears to maximum on the Korean Peninsula southeast seashore and Japanese southeast seashore. In the Korean Peninsula surrounding sea area, sea surface temperature and air temperature difference appeared high at the ES and appeared low at the YS. This is because longwave radiation is function of temperature difference.

Shortwave radiation decreases as is going to high latitude in winter and is bigger relatively than winter in summer. Because this

is smaller cloudiness values of the summer season. Because incoming shortwave radiation is influenced greatly according to solar altitude, is shown distribution that decrease as go to high latitude, and the values cause in difference of cloudiness.

Among research periods, it is analyzed for changing pattern sensible heat and latent heat flux, and turbulent kinetic energy (TKE) through case study. When sea surface temperature increases, sensible heat flux decreased and latent heat and turbulent kinetic energy increased. Because this was very small results relatively than increase of latent heat flux even if sensible heat flux decreased in turbulence energy equation, Finally, turbulent kinetic energy is increasing regardless of sensible heat flux.

The results of this study, the new algorithm of estimating heat flux from air temperature and specific humidity over the sea surface, are expected to be of much help for the studies of ENSO as well as for understanding and improved modelling of atmospheric and ocean circulation.

VI. References

- Ahn, J. B., J. H. Ryu., E. H. Cho., and J. Y. Park, 1997: A Study of Correlations between Air-Temperature and Precipitation of Korea and SST around Korean Peninsula. J. Korean Meteor. Soc., 33(2), 327-336.
- Arya, S. P., 1988: Introduction to Micrometeorology. Academic Press, 307 pp.
- Bennartz, Ralf, 1999; On the Use of SSM/I Measurements in Coastal Regions. Journal of Atmospheric and Oceanic Technology. 16, 417-431.
- Berliand, M. E. and T. G. Berliand, 1952: Determining the net long-wave radiation of the earth with consideration of the effect of cloudiness., Izv. Akad. Nauk. SSSR Ser. Geofiz., No. 1.
- Brown, J. W., O. B. Brown, and R. H. Evans, 1993: Calibration of AVHRR infrared channels: A new approach to non-linear correction. J. Geophys. Res., 98, 18257-18268.
- Budyko, M. I., 1974; Climate and Life., Academic Press, 508 pp.
- Bunker, A. F., 1976: Computations of surface energy flux and annual air-sea interaction cycles of the North Atlantic Ocean. Mon. Wea. Rev., 104, 1122-1139.
- Chou, M. D., P.-K. Chan and M. M.-H. Yan, 2001: A sea surface radiation data set for climate applications in the

- tropical western Pacific and South China Sea. *J. Geophys. Res.*, 106, 7219-7228.
- Chou, S. H., R. M. Atlas, C. L. Shie, and J. Ardizzone, 1995: Estimates of surface humidity and latent heat fluxes over oceans from SSM/I data. *Mon. Wea. Rev.*, 123, 2405-2425.
- Clark, N. E., L. Eber, R. Laurs, J. Renner and J. Saur., 1974: Heat exchange between ocean and atmosphere in the eastern North Pacific for 1961-1971, NOAA Tech. Rep. NMFS SSRF-682.
- Gautier, C., Peterson and C. Jones, 1998: Ocean surface air temperature derived from multiple data sets and artificial neural network. *Geophys. Res. Lett.*, 25, 4217-4220.
- Goodberlet, M. A., C. T. Swift, and J. C. Wilkerson, 1989: Remote Sensing of ocean surface winds with the Special Sensor Microwave/Imager. *J. Geophys. Res.*, vol. 94(C10), 14547-14555.
- Hackert, E. C., A. J. Busalacchi and R. Murtugudde, 2001: A wind comparison study using and ocean general circulation model for the 1997-1998 Elnino. *J. Geophys. Res.*, 106, 2345-2362.
- Halpern, D., V. Zlotnicki, J. Newman, O. Brown, and F. Wentz, 1994: An atlas of monthly distributions of GEOSAT sea surface height, SSM/I surface wind speed, AVHRR/2 sea surface temperature, and ECMWF surface wind components

- during 1988. Jet Propulsion Laboratory Publication 91-8, 110 pp.
- Hirose, N., 1995: Heat budget in the neighboring seas around Japan. Master's Thesis, Kyushu Univ., 142 pp.
- Hirose, N., H. C. Lee and J. H. Yoon, 1999: Surface heat flux in the East China Sea and Yellow Sea. *J. Phys. Oceanogr.*, 29, 401-417.
- Hsiung, J., 1986: Mean surface energy fluxes over the global ocean. *J. Geophys. Res.*, 91, 10585-10606.
- Ishii, T., and J. Kondo, 1987: Seasonal variation of the heat balance of the East China Sea, *Tenki*, 34, 517-526.
- Jang J. D., Suh A. S., Kim Y. S. and Lee Y. S., 1997: Study on the retrieval oceanic surface wind speed around Korea using SSM/I data. *Journal of Atmospheric Research*. 14, 29-33.
- Jang, J. D., Kim, Y. S., Kang, S. C, and Chung, H. S, 1999: Evaluation of Latent and Sensible Heat Fluxes over the Oceans around the Korean Peninsula Using Satellite Data. *J. Korean Meteor. Soc.*, 2, 29-34.
- Jones, C., P. Peterson and C. Gautier, 1999: A new method for deriving ocean surface specific humidity and air temperature: An artificial neural network. *J. Appl. Meteorol.*, 38, 1229-1245.
- Kang, I. S., M. K. Kim and T. B. Shim, 1994: Seasonal variation of surface heat budget and wind stress over the seas around the Korean Peninsula. *J. Oceanol. Soc. Korea*,

- 29, 325-337.
- Kato, K., and T. Asai, 1983: Seasonal variations of heat budgets in both the atmosphere and the sea in the Japan Sea area. *J. Meteor. Soc. Japan*, 61, 222-238.
- Kim, Y. S., 1992: Estimate of heat transport across the sea surface near Japan with bulk methods. Doctoral Thesis, Univ. of Tokyo, 124 pp.
- Kim, Y. S. and R. Kimura, 1995: Error evaluation of the bulk aerodynamic method for estimating heat flux over the sea. *J. Korean Meteor. Soc.*, 31, 399-413.
- Kim, Y. S. and B. H. Kwon, 2003: Variations of Heat Fluxes over the East China Sea and the Southern Part of the East Sea Based on the Buoy Data. *J. Korean Meteor. Soc.*, 39, 337-345.
- Konda, M., 1996: Air-sea heat flux near Japan determined by satellite observations(in Japanese), M. S. thesis, Kyoto Univ., Kyoto, Japan.
- Kondo, J., 1975: Air-sea bulk transfer coefficients in diabatic conditions. *Boundary Layer Meteorol.* 9, 91-112.
- , 1976: Heat balance of the East China Sea during the air mass transformation experiment. *J. Meteor. Soc. Japan*, 54, 382-398.
- Kubota, M. and Mitsumori, S., 1995: Sensible Heat Flux Estimated by using Satellite data over the North Pacific.

J. Meteor. Soc. Japan

Kubota, M., N. Iwasaka, S. Kizu and M. Konda, 2002: Japanese Ocean Flux Data Sets with Use of Remote Sensing observation (J-OFURO). *J. Ocenogr.* 58, 213–225.

Lee, S. W., 1999: The Book of the Korean adjacent Sea. Jibmoon company, 334pp.

Liu, W. T., 1986: Statistical relation between monthly precipitable water and surface-level humidity over global oceans. *Mon. Wea. Rev.*, 114, 1592–1602.

——, and F. J. Wentz, 1992: Precipitable water and surface humidity over global oceans from Special Sensor Microwave Imager and European Center for Medium Weather Forecasts. *J. Geophys. Res.*, 97, 2251–2264.

McClain, E. P., W. G. Pichel, and C. C. Walton, 1985: Comparative Performance of AVHRR-Based Multichannel Sea Surface Temperature. *Journal of Geophysical Research*, 92, 11,587–11,601.

Na, J. Y., J. W. Seo, and H. J. Lie, 1999: Annual and seasonal variations of the sea surface heat fluxes in the East Asian Marginal Seas. *J. Ocenogr.*, 55, 257–270.

Park, W. S., I. S. Oh and T. B. Shim, 1995: Temporal and spatial distributions of heat fluxes in the East Sea (Sea of Japan). *J. Oceano. Soc. Korea*, 30, 91–115.

Prihodko, L. and S. N. Groward, 1997: Estimation of air

- temperature from remotely sensed surface observations. *Remote Sens. Environ.*, 60, 335-346.
- Reed, R. K., 1996: An evaluation of cloud factors for estimating insolation over the ocean. NOAA Tech. Memo. ERLPMEL-8P, 20 pp.
- Reynolds, R. W., and T. M. Smith, 1994: Improved global sea surface temperature analyses using optimum interpolation. *J. Climate*, 7, 929-948.
- Schussel, P., L. Schanz, and G. Englisch, 1995: Retrieval of 1 latent heat flux and longwave irradiance at the sea surface from SSM/I and AVHRR measurements. *Adv. Space Res.*, 16, 107-116.
- , P., J. Schulz, J. Meywerk, and S. Ewald, 1997: Evaluation of satellite-derived latent heat fluxes. *J. Climate*, 10, 2782-2795.
- Schulz, J., P. Schussel, and H. Grabl, 1993: Water vapour in the atmospheric boundary layer over oceans from SSM/I measurements. *Int. J. Remote Sens.*, 14, 2773-2789.
- Seckel, G. R., and F.H. Beaudy, 1973: The relationship between sun and sky over the North Pacific Ocean (abstract). *Trans. Amer. Geophys. Union*, 54, 1114pp.
- Shibata, A., 1992: Verifications of geophysical parameters retrieved by the Special Sensor Microwave/Imager and analysis of variations discerned in these data in the tropics,

- Umi to Sora, 67, 295-312.
- Shibata, A. and Konda, M., N., 1996: A new method to determine near-sea surface air temperature by using satellite data. *J. Geophys. Res.*, 101, 14349-14360
- Stull, R., 1995; *Meteorology Today for Scientist and Engineers*. West Publishing Company, 504pp.
- Ulaby, F. T., Moore, R. K. and Fung A. K., *Microwave Remote Sensing Active and Passiv*, Vol. 3. Norwood, MA. Artech, 1986, 1440-1467.
- Wallace, J. M and M. L. Blackmon, 1983: Observation of low-frequency atmospheric variability. large-scale dynamic precesses in the atmosphere, R. J. Hoskin and R. D. Peare Eds., Academic Press, 55-94.
- Wentz, F. J., 1992; *Measurement of Oceanic Wind Vector Using Satellite Microwave Radiometers*, RSS Technical Report 051591, 33, Remote Sensing Systems, Santa Rosa, CA, 15
- Wents, F. J., 1997: A well-calibrated ocean algorithm for SSM/I. *J. Geophys. Res.*, 102, 8703-8718.
- Yu, T.-W., M. Iredell, D. Keyser, 1997; *Global Data Assimilation and Forecast Experiments Using SSM/I Wind Speed Data Derived from a Neural Network Algorithm*. *Weather and Forecasting*. 12, 859-865.